

The evolution of velocity dispersion in the Sco-Cen OB association

Josefa E. Großschedl^{1,2,3}, João Alves^{3,4}, Sebastian Ratzenböck⁵, Núria Miret-Roig^{3,6,7}, Alvaro Hacar³, Sebastian Hutschenreuter³, and Laura Posch³

¹ Astronomical Institute of the Czech Academy of Sciences, Boční II 1401, 141 31 Prague 4, Czech Republic,
e-mail: grosschedl@asu.cas.cz

² Universität zu Köln, I. Physikalisches Institut, Zülpicher Str. 77, 50937 Köln, Germany

³ University of Vienna, Department of Astrophysics, Türkenschanzstraße 17, 1180 Vienna, Austria

⁴ University of Vienna, Data Science at Uni Vienna Research Platform, Austria

⁵ Center for Astrophysics | Harvard & Smithsonian, 60 Garden St., Cambridge, MA 02138, USA

⁶ Dep. de Física Quàntica i Astrofísica (FQA), Univ. de Barcelona (UB), Martí i Franquès, 1, 08028 Barc., Spain

⁷ Institut de Ciències del Cosmos (ICCUB), Univ. de Barcelona (UB), Martí i Franquès, 1, 08028 Barcelona, Spain

Received May 14, 2025 ; Resubmitted September 23, 2025; Accepted ...

ABSTRACT

We study how stellar velocity dispersion within the Scorpius-Centaurus OB association (Sco-Cen) has evolved over approximately 20 million years, from its formation to the present day. Using data from the *Gaia* mission along with supplementary stellar radial velocities, we identified a surprising sequence of abrupt jumps and intervening plateaus in the velocity dispersion correlating with star formation bursts. These changes in velocity dispersion coincide with the association expanding in size. We measure a present-day expansion rate of about 10–12 pc Myr⁻¹ and observe that younger star clusters within the association exhibit higher velocities compared to older ones. This result, along with the stepwise increase in both velocity dispersion and spatial extent over time, suggests a structured and sequential star formation process rather than a random one. This phased evolution strongly suggests that stellar feedback is the primary driver of Sco-Cen’s star formation history, expansion, and eventual dispersal. Our findings emphasize the value of precisely characterizing stellar populations within OB associations, particularly through the creation of detailed, high-resolution age maps.

Key words. Methods: data analysis – Stars: kinematics and dynamics – Galaxy: open clusters and associations: individual: Sco-Cen

1. Introduction

Understanding the temporal evolution of OB associations is crucial for understanding the role of massive stars in shaping their environments (e.g., [Brown et al. 1997](#)). OB associations represent an essential, yet transient phase in the life cycle of massive stars and star-forming regions (e.g., [Blaauw 1964a](#); [Wright et al. 2023](#)). The traditional view of OB associations has been significantly refined with *Gaia* data ([Gaia Collaboration et al. 2016](#)). Recent *Gaia*-based studies reveal that OB associations comprise dozens of largely unbound stellar populations with ages up to roughly 20 Myr (e.g., [Kos et al. 2019](#); [Chen et al. 2020](#); [Kerr et al. 2021](#); [Ratzenböck et al. 2023b](#); [Hunt & Reffert 2023](#)), rather than just a few subgroups. Moreover, they are likely linked to even larger and older cluster families, which could trace their origins to spiral arm activity ([Swiggum et al. 2024, 2025](#)).

A comprehensive characterization of stellar groups within OB associations is crucial for understanding their formation mechanisms and boundness state, as they ultimately disperse and merge with the field star population (e.g., [Lynga & Palous 1987](#); [Kamaya 2004](#)). OB associations also provide insights into star formation mechanisms, stellar feedback, and early dynamical evolution. Their velocity dispersion is a key factor, which provides insights into the internal motions, dynamical states, and evolutionary histories of stellar populations, eventually shaping the structure of the Galactic field population (e.g., [Lada et al. 1984](#); [Lada & Lada 2003](#); [Kroupa 1995, 2008](#); [de la Fuente Marcos & de la Fuente Marcos 2008](#); [Kuhn et al. 2019](#)).

Although velocity dispersion is widely recognized as a fundamental population property, its temporal evolution during the formation of a single stellar association remains largely unexplored. Previous observational studies provide only snapshots in time, which limit our understanding of how stellar populations evolve dynamically. The lack of observational data on the temporal evolution of velocity dispersion represents a major gap in our understanding of stellar population formation.

To address this, we use high-precision *Gaia* DR3 data ([Gaia Collaboration et al. 2023](#)), supplemented with ancillary radial velocity (RV) measurements, to investigate the temporal evolution of velocity dispersion in the Scorpius-Centaurus OB association (Sco-Cen; e.g., [Blaauw 1964a,b](#); [Preibisch & Mamajek 2008](#)). This study builds on the recent identification of more than 30 coeval and comoving stellar clusters¹ within Sco-Cen with ages of approximately 3 to 21 Myr (see [Ratzenböck et al. 2023a,b](#); [Miret-Roig et al. 2025](#), hereafter, [R23a](#), [R23b](#), [MR25](#)). These studies identified spatio-temporal patterns, using high-resolution age maps, indicative of sequential star formation. This enabled the identification of cluster chains with well-defined age, mass, position, and velocity gradients extending outward at the periphery of the association (see [Posch et al. 2023, 2025](#), hereafter, [P23](#), [P25](#)). In this paper, we aim to reconstruct, for the first time, the temporal evolution of velocity dispersion and internal motions of an OB association by analysing 32 well-defined clusters in the 6D phase space over a time span of about 20 Myr.

¹ We use the term “cluster” in a statistical sense, as in [R23a](#).

2. Data

We use the Sco-Cen cluster sample from R23a, which was selected with the unsupervised machine-learning tool **SigMA** (Significance Mode Analysis), containing 34 clusters related to Sco-Cen. We add two clusters from the TW Hydreae association (TWA), which are connected to Sco-Cen as a cluster chain (see MR25). The combined sample contains a total of 13,011 stellar members. R23b determined cluster ages by fitting PARSEC model isochrones (Bressan et al. 2012) with a Bayesian inference approach. We use the isochronal ages fitted to the *Gaia* colour–absolute-magnitude diagram G_{abs} vs $G_{\text{BP}} - G_{\text{RP}}$. MR25 estimate the cluster ages of TWA-a,b consistently with the same method as R23b. The Sco-Cen clusters cover ages from about 3 to 21 Myr, and are used as time information in our analysis. A detailed data description is given in Appendices A.1 & A.2.

To study the clusters in 6D phase space, we combine the astrometric 5D data with RV data. *Gaia* DR3 provides RV measurements (Katz et al. 2023) for about 38% of our sources, however, only about 11% have relatively low uncertainties ($e_{\text{RV},\text{Gaia}} < 3.1 \text{ km s}^{-1}$)² with a median error of about 1.5 km s^{-1} . Moreover, some of the relatively sparse clusters contain no or very few stars with *Gaia* RVs. Hence, we add supplementary RV data from 22 spectroscopic surveys (see Appendix A.3 & Table A.1). After the cross-match, about 50% of the sources have RV measurements from at least one survey. To determine robust 3D space motions, we apply several cleaning steps, including a cut using the cluster stability value from R23a, an RV error cut at $e_{\text{RV}} < 3.1 \text{ km s}^{-1}$, removal of binary candidates, and a global outlier cut and 3σ -clipping, as outlined in detail in Appendix A.4. Finally, our RV sample contains about 25% of the original stellar sample (3222/13,011). The median RV error is of this sample is about 0.3 km s^{-1} (min/max = $0.015/3.05 \text{ km s}^{-1}$). A detailed overview of the data statistics per cluster is given in Table A.2.

Eventually, we use 32 out of the 36 Sco-Cen clusters. We find that the sparse cluster μ Sco has very poor RV statistics, and we remove it from further analysis in this work. Moreover, we remove three clusters from the Chamaeleon-Musca-Coalsack region (Cham-I, Cham-II, Cen-Far). They are slightly detached from Sco-Cen and probably belong to a background structure, called the “C” (Edenhofer et al. 2024b). The remaining 32 analysed clusters contain a total of 12,612 stellar candidate members, while we also report statistics for the four removed clusters in Table A.2.

3. Methods

We calculate the velocity dispersion from the stellar members of the clusters in 3D, using the Galactic Cartesian velocities (UVW , see Appendix A.2), after applying the quality criteria from Appendix A.4:

$$\sigma_{3\text{D}} (\text{km s}^{-1}) = \sqrt{\sigma_U^2 + \sigma_V^2 + \sigma_W^2} \quad (1)$$

The one-dimensional velocity dispersions ($\sigma_{U,V,W}$) were calculated via the standard deviation in the three velocity spaces. We use the time information (cluster ages) to investigate the evolution of velocity dispersion in 3D. This is possible for the first time, since we have a coherent sample of clusters, which formed in a single OB association with a wide range of ages and with 3D information.

² As in our quality criteria (Appendix A.4); chosen to ensure that also sparse clusters contain several stars with measured RVs.

We calculate $\sigma_{3\text{D}}$ cumulatively by progressively incorporating member stars of the next younger stellar population at each time step for its calculation. In other words, we start the calculation of the cumulative $\sigma_{3\text{D}}$ with only the stellar members of the oldest cluster (e Lup), then add the stars of the next youngest cluster at each step, and finally, we end with all member stars from all studied clusters. We calculate the cumulative $\sigma_{3\text{D}}$ by iteratively picking equal subsamples from each cluster at each timestep, to account for the different cluster sizes, as detailed in Appendix B.1.

Next, we similarly estimate the spatial stellar build-up of Sco-Cen in chronological order. To this end, we determine the maximum cluster extent (S , size in pc) as observed today, by measuring the minimal distance across the connections using a k-nearest neighbour graph of the member stars in the XYZ space. We construct this graph from individual stellar members as nodes and we use Dijkstra’s algorithm to compute the shortest paths between any two sources along the edges of this graph. Thus, at each step, we compute the maximally possible path distance that you can take between any two pairs of Sco-Cen member stars older than the given age step. More details are given in Appendix B.2. The presented chronological stellar build-up is not exactly the same as the evolution of size over time, since we do not include orbital tracebacks of the clusters at this stage. The present-day change in extent is used as a reference quantity, and it should give a more quantitative visualization of the spatial build-up as also shown in Fig. 2. We will look into a more detailed traceback analysis in future work, where various second order effects and required assumptions will be taken into account (e.g., cluster expansion, acceleration from feedback, non-sphericity, Galactic potential, possible internal gravitational effects, orbit integration with different Solar parameters).

We further investigate the clusters’ 3D bulk positions and motions, using the cluster medians in Galactic Cartesian coordinates (XYZ) and velocities (UVW). The corresponding uncertainties are determined by bootstrap sampling from the cluster members (Appendix B.3). We calculate the position and velocity vectors for each cluster relative to a chosen centre (XYZ_{ctr}) and rest velocity (UVW_{rest}):

$$\begin{aligned} \mathbf{r} &= ((X - X_{\text{ctr}}), (Y - Y_{\text{ctr}}), (Z - Z_{\text{ctr}})) \\ \mathbf{v} &= ((U - U_{\text{rest}}), (V - V_{\text{rest}}), (W - W_{\text{rest}})) \end{aligned} \quad (2)$$

Next, we calculate the relative distances of the clusters (r , vector norm, in pc) and the relative velocities (v , or speed, in km s^{-1}), via the Euclidean distance in position and velocity space to the given reference point.

$$\begin{aligned} r &= \|\mathbf{r}\| = \sqrt{(X - X_{\text{ctr}})^2 + (Y - Y_{\text{ctr}})^2 + (Z - Z_{\text{ctr}})^2} \\ v &= \|\mathbf{v}\| = \sqrt{(U - U_{\text{rest}})^2 + (V - V_{\text{rest}})^2 + (W - W_{\text{rest}})^2} \end{aligned} \quad (3)$$

We determine the radial component of the velocities relative to the chosen reference point as follows:

$$v_r = \frac{\mathbf{r} \cdot \mathbf{v}}{r} \quad (4)$$

The tangential component is then computed with:

$$v_{\text{tan}} = \sqrt{v^2 - v_r^2} \quad (5)$$

To define the reference point (centre and rest velocity), we use three approaches to investigate possible systematics. The centre of Sco-Cen is not a well-defined point and depends also on the question at hand (e.g., centre of feedback, centre of mass, or using older clusters to find the point of first star formation).

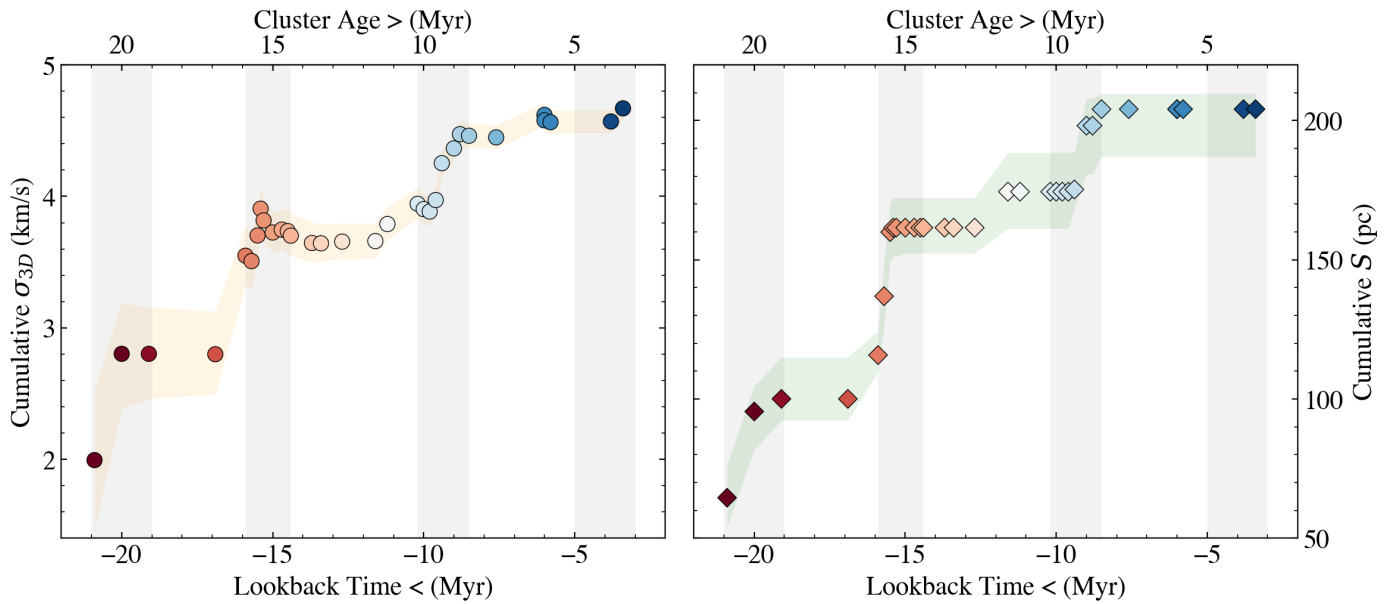


Fig. 1. Temporal evolution of the cumulative 3D velocity dispersion (σ_{3D} , left panel) and present-day cumulative spatial extent (S , right panel), using the cluster ages as time information. The orange and green shaded areas are the 95% interquartile ranges (2σ bound), highlighting the uncertainties of the two trends. The symbols are colour-coded by the formation time of the youngest cluster included (correlates with the x-axis). The four vertical grey bars indicate the four main star formation events in Sco-Cen; periods of increased star formation rate, as discussed in R23b (see their Fig. 3).

First, we use the median position and motion of the oldest cluster in the region, e Lup (age about 21 Myr), which is located at a central position. We assume that its velocity is reminiscent of the original velocity of the primordial star-forming molecular cloud when the first stars formed. Additionally, we use the cluster ϕ Lup, another central cluster in Sco-Cen with an age of about 17 Myr, which is connected to two chains of clusters (see P23; P25). Finally, we use the median motion of the stellar members of the oldest clusters in Sco-Cen with ages > 15 Myr, denoted as $SC15$, to get another estimate of the bulk motion of the early star-forming region (see similar approaches in P25 and MR25). More details on the determination of $SC15$ and a comparison of the three chosen centres (e Lup, ϕ Lup, $SC15$) are given in Appendix B.4.

We further investigate the biasing effects from choosing different reference points in our subsequent analysis by using each of the 32 Sco-Cen clusters once as a reference point. This creates cases that are not time-ordered or that are starting from a non-central location, as detailed in Appendix B.5.

4. Results

4.1. Cumulative velocity dispersion and extent

Figure 1 (left panel) shows the cumulative 3D velocity dispersion σ_{3D} of Sco-Cen as a function of cluster age (or lookback time). We observe a general increase in velocity dispersion over time, with a pattern of jumps and plateaus, reaching a final value of 4.67 ± 0.04 km s $^{-1}$. This cumulative value is determined by iterating over equally sized sub-samples within each cluster (Appendix B.1). For comparison, the total σ_{3D} , calculated using all stellar members of Sco-Cen that meet our quality criteria (without sub-sampling), yields a value of 3.96 ± 0.03 km s $^{-1}$. The different values of the total 3D velocity dispersion are caused by the sub-sampling approach that we use for the cumulative σ_{3D} , in order to give similar weight to each cluster, while in the case

when using all available stars, the more massive clusters might dominate the total σ_{3D} . Moreover, the iterative sub-sampling approach likely creates some under-sampling of the velocity space, which gives more weight to individual measurement errors, artificially inflating the velocity dispersion, while the shape of the cumulative trend appears unaffected, as demonstrated in the following paragraph and in more detail in Appendix B.1.

We test the shape of the cumulative trend by calculating the cumulative σ_{3D} , first, by applying stricter error cuts ($e_{RV} < 1$ km s $^{-1}$), and second, by using the UVW medians of the 32 clusters instead of individual stars. In the first case, we get a total velocity dispersion of 4.46 ± 0.03 km s $^{-1}$, and in the second case 4.17 ± 0.07 km s $^{-1}$. Additionally, we test the effect of binaries that might be contained in our sample, using the $Gaia$ RUWE parameter to roughly exclude binary candidates, which results in effectively the same trend as in Fig. 1. Generally, all tests produce similar increasing trends of the cumulative σ_{3D} over time, while only the magnitude of σ_{3D} gets shifted (see Appendix B.1 & Fig. B.1)

We conclude that the whole Sco-Cen association has a 3D velocity dispersion of approximately $4\text{--}4.7$ km s $^{-1}$, whereas individual clusters within the association have significantly smaller dispersions, on the order of $1\text{--}2$ km s $^{-1}$ (we discuss the individual clusters' velocity dispersions in future work). We find that the shape of the cumulative σ_{3D} is largely unaffected by measurement errors or binaries, since only the magnitude of the σ_{3D} values shifts consistently to somewhat lower values when applying more conservative cuts (see Fig. B.1).

Figure 1 (right panel) shows similarly the present day chronological build-up of Sco-Cen (S , pc) as observed today, also calculated cumulatively starting with the oldest cluster. The total extent of the association is about 203^{+7}_{-12} pc, when calculated with the method described in Appendix B.2. The size increases when adding stars from clusters ordered by their age, which is consistent with the visible spatio-temporal patterns identified in R23b (Fig. 2) and the cluster chains discussed in P23; P25; and

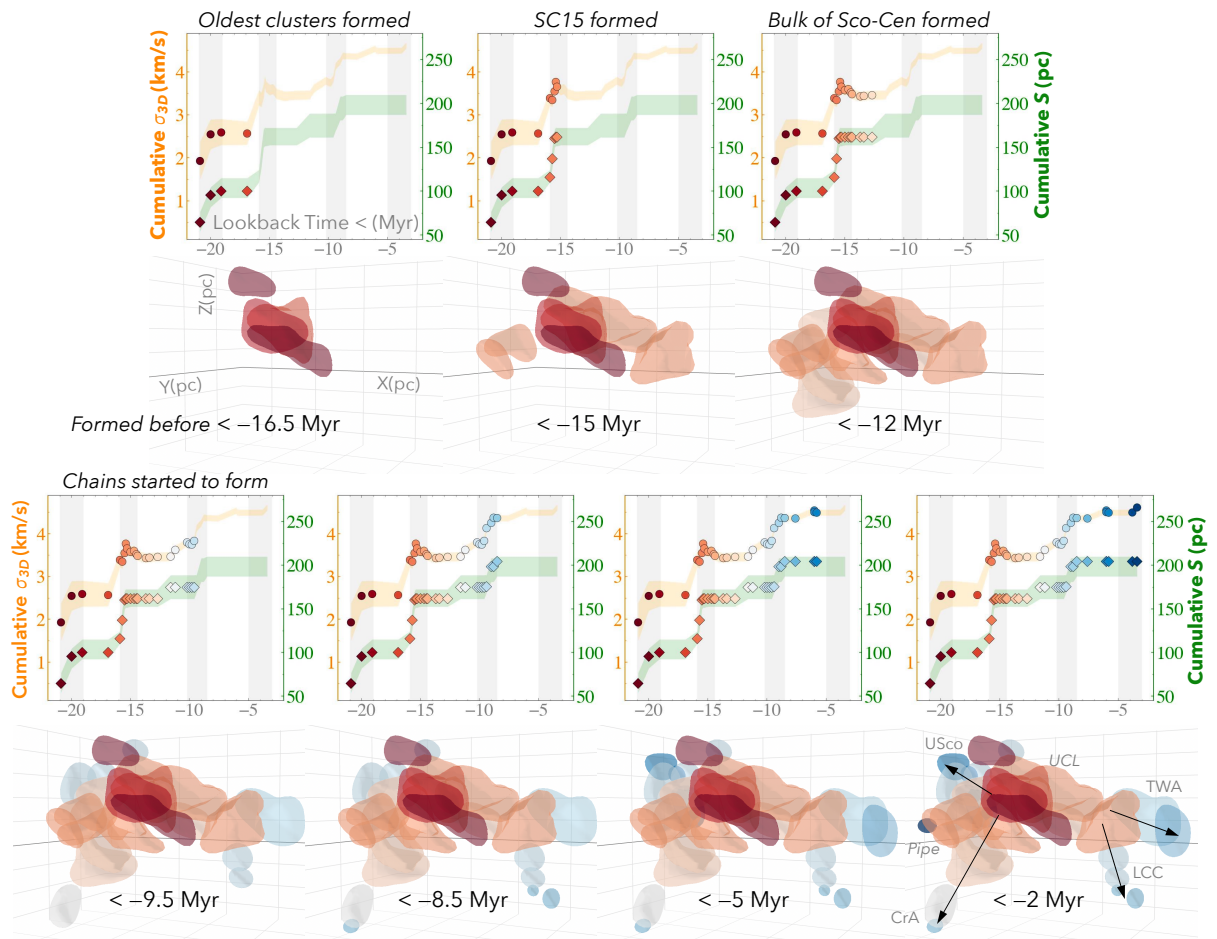


Fig. 2. Spatio-kinematical build-up of Sco-Cen, illustrating how velocity dispersion and spatial extent change when using the cluster ages as time information. The upper panels display the cumulative 3D velocity dispersion and extent, similar to Fig. 1, but shown here in one plot with split y-axes. At each of the seven time-steps, only the clusters that formed before the indicated formation times are considered. Below each graph, seven 3D age maps depict the spatial distribution of clusters (in XYZ), showing clusters (as age-coloured surfaces) that formed before the indicated time thresholds, highlighting which clusters contribute to the changes in σ_{3D} . Sub-regions and cluster chains are labelled in the final panel. The 3D visualizations originate from the studies R23b and MR25; interactive versions are available in the respective publications.

MR25. These studies propose an inside-out formation history, which was also suggested earlier for Sco-Cen (e.g., Preibisch & Zinnecker 1999; Gaczkowski et al. 2017; Krause et al. 2018). Moreover, we see that the cumulative size increases similarly to the cumulative σ_{3D} , as discussed further in Sect. 5.4.

Figure 2 highlights the evolution of velocity dispersion and size in more detail. It shows the build-up of Sco-Cen after seven formation times. In this combined view, it becomes clear that the increasing velocity dispersion and size of Sco-Cen are connected by an evolutionary pattern, from the inside out. Changes appear when star formation proceeds to an adjacent gas reservoir; notably, the onset of the formation of the cluster chains correlates with an increase and jump in σ_{3D} . To further investigate the origin of the increase in the velocity dispersion and the spatio-temporal evolution of Sco-Cen, we look in more detail into the relative 3D space motions and positions of the Sco-Cen clusters in the following section.

4.2. Correlation of time, cluster motion, and position

Figure 3 shows the cluster speed (v) versus the time of cluster formation (t), denoted as the look-back time, with the oldest cluster, e Lup, as a reference point. We find a linear relation between speed and time, with the resulting fitting param-

eters reported in Table 1. The slope of the relation is about $0.45 \text{ km s}^{-1} \text{ Myr}^{-1}$, where younger clusters have a systematically higher relative speed. The intercept gives about 11 pc Myr^{-1} (units converted from km s^{-1}), which could be interpreted as expansion velocity at the present day. However, the speed calculated in this manner (Eq. (3)) does not give information about the direction of motion; therefore, we also dissect the relative motions into a radial and tangential component (Eqs. (4–5)).

Figure 4 shows the radial component of the relative cluster motions (v_r) versus relative distance (r), again with e Lup as reference point. First, we find that the majority of clusters have positive values in v_r , which shows that most of them are moving away from the central cluster e Lup, while younger clusters tend to have higher radial outward motions. Only one of the older and the most massive clusters at the centre of Sco-Cen shows a slightly negative component, which is v Cen with $v_r \sim -0.12 \text{ km s}^{-1}$. Second, we find a clear linear trend, where v_r increases with r . We fit a linear regression to the data points, only using clusters with $v_r > 0$ (excluding e Lup and v Cen). This delivers a slope of about $0.09 \text{ km s}^{-1} \text{ pc}^{-1}$, named radial-motion–distance relation (see Table 1). Hence, clusters at larger distances from the centre tend to have higher velocities radially away from it, suggesting an outward expansion, reminiscent of a Hubble flow. The inverse of the slope gives a time of about

Table 1. Linear fitting results (slope a , intercept b) of the speed (v) versus time (t) and radial-motion (v_r) versus distance (r) relations when using three different reference points (see Figs. 3, 4, B.2, and B.3).

Reference Point	speed-time relation			radial-motion-distance relation		
	$v = b + a \cdot t$			$v_r = b + a \cdot r$		
	$a = \frac{dv}{dt}$ km s ⁻¹ Myr ⁻¹	b km s ⁻¹	b pc Myr ⁻¹	$a = \frac{dv_r}{dr}$ km s ⁻¹ pc ⁻¹	b km s ⁻¹	a^{-1} Myr
e Lup (20.9 Myr)	$0.45^{+0.08}_{-0.07}$	$10.55^{+0.87}_{-0.85}$	10.8 ± 0.9	$0.092^{+0.009}_{-0.009}$	$-2.01^{+0.55}_{-0.60}$	$10.6^{+1.2}_{-1.0}$
ϕ Lup (16.9 Myr)	$0.42^{+0.07}_{-0.06}$	$9.54^{+0.84}_{-0.82}$	9.8 ± 0.9	$0.082^{+0.010}_{-0.010}$	$-1.28^{+0.56}_{-0.54}$	$12.0^{+1.7}_{-1.3}$
SC15 (>15 Myr)	$0.34^{+0.06}_{-0.06}$	$8.44^{+0.71}_{-0.71}$	8.6 ± 0.7	$0.072^{+0.011}_{-0.010}$	$-0.91^{+0.58}_{-0.68}$	$13.7^{+2.4}_{-1.8}$

Notes. Col. 1 lists the three chosen reference points, with the cluster age in brackets or the age cut in the case of SC15. The slope of the speed–time relation gives the expansion over time (Col. 2). The intercept of the speed–time relation gives the expansion speed of Sco-Cen at the present day, given in km s⁻¹ in Col. 3, converted to pc Myr⁻¹ in Col. 4. In Col. 7, the inverse of the slope of the radial-motion–distance relation gives the time of the possible onset of the expansion.

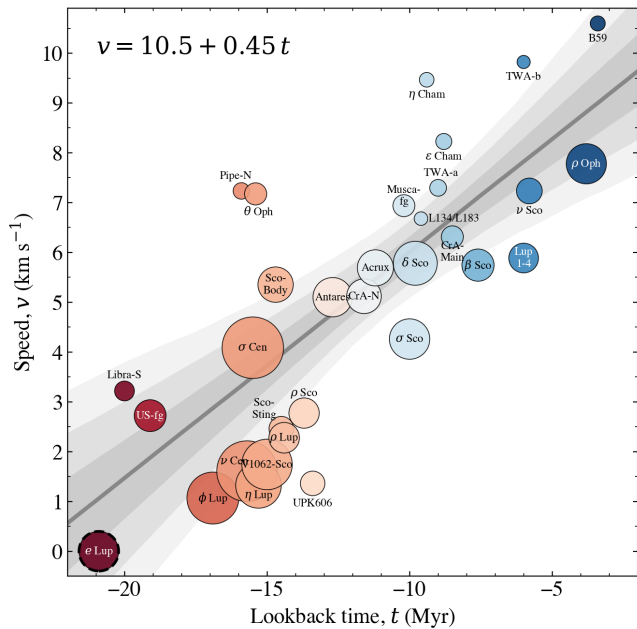


Fig. 3. Speed–time relation. Relative cluster speed (v) versus lookback time (t), with the oldest cluster (e Lup) as reference point that is excluded from the linear fit (black, dashed circle). The symbols are colour-coded by formation time (or cluster age, see x-axis) and scaled by number of sources per cluster. The linear fit (grey, solid line) is obtained via bootstrapping, with the median fitting parameters given in the upper left corner. The fit uncertainties are plotted as grey shaded areas (1-2-3- σ).

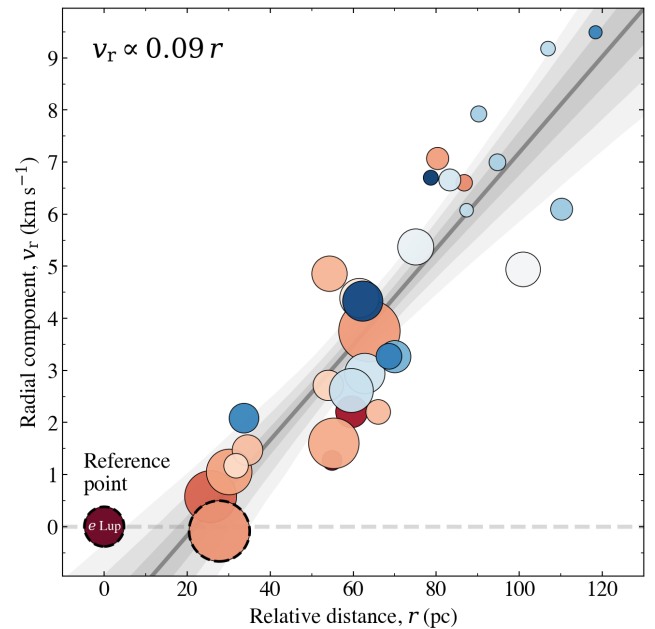


Fig. 4. Radial-motion–distance relation. Radial component of the relative cluster motions (v_r) versus relative cluster distance (r), with e Lup as reference point. The symbols are colour-coded by formation time, as in Fig. 3. A linear fit to the data is shown as a grey solid line, with the best fitting slope given in the upper left corner, and the 1-2-3- σ fit uncertainties are plotted as grey shaded areas. The two clusters marked by black, dashed circles (e Lup, v Cen) are excluded from the linear fit.

11 Myr. This can be interpreted, to first order, as the approximate time of the onset of significant radial expansion, assuming no external forces.

We repeat the same analysis with two alternative reference frames—using ϕ Lup and SC15, instead of e Lup (see Sect. 3 and Appendix B.4)—to test the robustness of the identified relations. For these two cases, we find similar trends with slightly shallower slopes, showing that the expansion patterns are valid from different reference points that are located at central locations (see Figs. B.2, B.3, & Table 1).

We further test the linear relations by setting each of the 32 clusters once as a reference point (see Appendix B.5). With this, we check if the older clusters at central locations (such as e Lup or ϕ Lup) are likely a centre of expansion, or if the expansion pattern is independent of the central area or of the age of the ref-

erence cluster (hence, independent of time). In most cases, the resulting correlations are less clear, showing more scatter and flatter slopes when compared to e Lup as reference point. We also test if the radial motions are positive for the majority of the clusters as reference points, since negative values indicate infalling motions. For some cases (mostly when using younger clusters as reference points), we find that several clusters now have negative v_r , which means that those reference points appear to create relatively in-falling motions instead of predominantly expanding motions, which suggests that these clusters are less likely to be the point of expansion. These test show us that independent of the reference frame, the association appears to be expanding radially in most cases, in particular when using clusters with ages > 12 Myr as reference, while the cleanest trend is created when using e Lup (see more details in Appendix B.5).

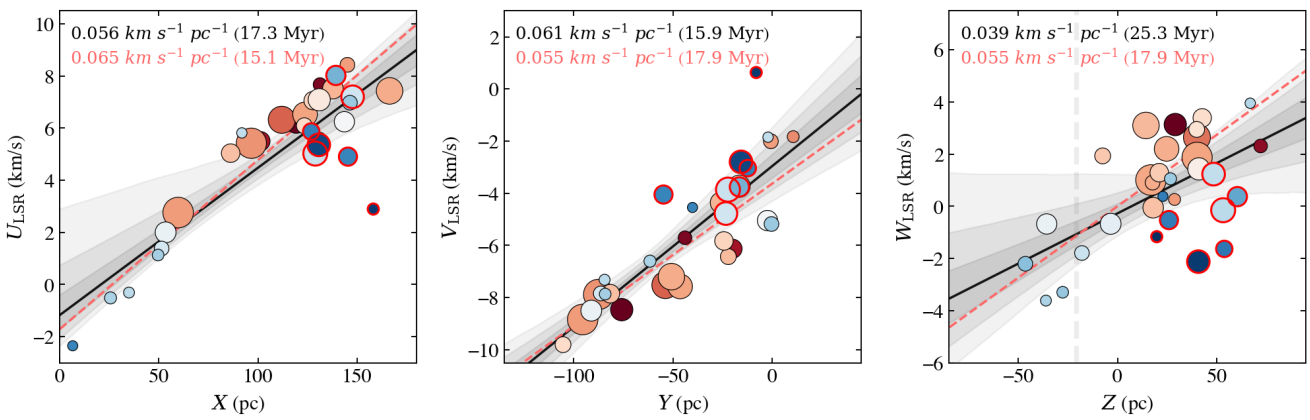


Fig. 5. Position velocity (PV) diagrams for the 32 Sco-Cen clusters using the XU , YV , and ZW spaces. Symbols and colours as in Fig. 3. The median slopes of the fitted linear regressions (black, solid lines) are given in the upper left corners. The grey shaded areas are the 1-2-3- σ uncertainty ranges. The inverse of the slope gives a time in Myr, in brackets. The red, dashed slopes are the linear fitting results when using only 25 clusters, after removing seven clusters with peculiar tangential motions, marked with red circles (see Sect. 5.2). In the ZW diagram (right panel), the vertical grey, dashed line indicates the approximate location of the Galactic mid-plane, assuming that the Sun is located about 21 pc above (e.g., Bennett & Bovy 2019).

Table 2. Linear regression results for the three PV diagrams (PWD), as shown in Fig. 5.

PWD	Slope (a)	Intercept (b)	Time (a^{-1})
	$\text{km s}^{-1} \text{ pc}^{-1}$	km s^{-1}	Myr
using 32 clusters	$0.056^{+0.006}_{-0.007}$	$-1.17^{+0.76}_{-0.53}$	$17.3^{+2.4}_{-1.9}$
	$0.061^{+0.006}_{-0.006}$	$-2.98^{+0.46}_{-0.45}$	$15.9^{+1.9}_{-1.5}$
	$0.039^{+0.009}_{-0.010}$	$-0.26^{+0.35}_{-0.32}$	$25.3^{+8.9}_{-5.2}$
using 25 clusters	$0.065^{+0.004}_{-0.005}$	$-1.72^{+0.53}_{-0.37}$	$15.1^{+1.2}_{-1.0}$
	$0.055^{+0.006}_{-0.007}$	$-3.63^{+0.44}_{-0.49}$	$17.9^{+2.3}_{-1.9}$
	$0.055^{+0.008}_{-0.008}$	$-0.01^{+0.32}_{-0.30}$	$17.9^{+3.4}_{-2.4}$

Notes. Top three rows: Results obtained by using all 32 clusters. Bottom three rows: Results obtained by using only 25 clusters, after removing seven clusters with peculiar motions.

To further test the statistical significance of the correlation of speed with time (Fig. 3), we randomize the order of the time-axis, as detailed in the Appendix B.5. We find that the probability of obtaining a similar linear relation is below 4σ . In other words, random (not time-ordered) cases tend to produce shallower or reverse slopes and/or larger scatter. This suggests that the Sco-Cen clusters did not form randomly and independently from each other, but rather sequentially via propagated star formation.

Additionally, we explore the expansion patterns using three position-velocity diagrams (PWD) in the three Cartesian directions, shown in Fig. 5. We use the clusters' median positions, XYZ , and space motions relative to the local standard of rest (LSR), UVW_{LSR} , named XU , YV , and ZW diagrams. The XU and YV diagrams show positive correlations of position with velocity, which again suggests a large-scale expansion of the whole region. The ZW diagram shows more scatter and a less clear trend, while position and velocity are generally positively correlated. We fit linear regressions to the data in the three spaces and report the medians and uncertainties in Table 2 (determined via bootstrapping).

Looking at the ZW diagram in more detail (right panel in Fig. 5), we find that some clusters appear to be outliers, located mainly in the Upper Scorpius (USco) region. The discrepancy

in the motion of these clusters correlates with an additional tangential component of motion relative to the reference point, observed for seven clusters, which is discussed in more detail in Sect. 5.2. When we remove these seven clusters, we find a clearer correlation and expansion pattern in ZW , while the trends in XU and YV remain similar (see Fig. 5 & Table 2). Nevertheless, we find that the radial component of motion versus relative distance of these seven odd clusters follows the same trend as the rest of the Sco-Cen clusters, as can be seen in Fig. 4.

5. Discussion

In this paper, we present the first measurement of the temporal evolution of stellar velocity dispersion within a young stellar population. By using high-precision *Gaia* data supplemented with additional RV data, we identified an unexpected series of jumps and plateaus in the evolution of the velocity dispersion over the formation period of the Sco-Cen OB association (approximately 20 Myr). These findings suggest that star formation within Sco-Cen did not occur randomly but is structured and sequential. The simplest interpretation of our results suggests a scenario in which stellar feedback plays a significant role in influencing the observed dynamic evolution of stellar populations within the association.

The surprising sequence of abrupt jumps and intervening plateaus in the cumulative σ_{3D} of the Sco-Cen association, the central finding of this paper, correlate with four distinct star formation bursts. The four periods of heightened star formation rate, as identified in R23b, are marked by vertical grey bars in Figs. 1 & 2. These periods are separated by about 5 Myr. These findings suggest a structured and sequential formation process for Sco-Cen, likely driven by stellar feedback. As illustrated in Fig. 2, the jumps occur when star formation transitions spatially to an adjacent region. The observed jumps can be interpreted as the addition of a new ensemble of younger clusters; these additional young clusters have been formed from a nearby gas reservoir (close to the existing population of stars) with a marginally different velocity.

The concept of bursts in star formation and the complex age structures within Sco-Cen has been a subject of extensive research in previous works. For instance, Slesnick et al. (2008)

investigated the USco subgroup, concluding that its low-mass population formed in a single burst approximately 5 Myr ago, with an age spread of less than 3 Myr, after accounting for observational uncertainties. While this suggested a relatively coeval formation at the time, the apparent age spread observed in their Hertzsprung-Russell diagrams highlighted the complexities of age determination. More recently, [Pecaut & Mamajek \(2016\)](#) conducted a comprehensive study across all three Sco-Cen subgroups, demonstrating that none of them are consistent with simple, coeval populations formed in single bursts. Instead, they found strong evidence for age gradients and a “multitude of smaller star formation episodes” throughout the association, suggesting a more complex and prolonged star formation history (recently confirmed, e.g., by [R23b](#)). Their work emphasized the presence of substructure and found larger intrinsic age spreads (e.g., ± 7 Myr for USco) when using revised age scales and accounting for various observational effects. Our current findings provide novel kinematic evidence for these multi-episodic or burst-like star formation events, demonstrating how these bursts manifest as distinct ‘stepwise’ increases in the collective velocity dispersion and spatial expansion of the association over time. This directly reinforces the understanding that Sco-Cen’s evolution is not monolithic but rather a phased assembly of spatially and kinematically distinct stellar populations.

This sequential progression in space and time, characterized by radially ordered outward motions rather than random (Figs. 3 & 4), suggests the presence of a coordinating agent. A plausible agent to create the observed order in cluster positions, ages, and motions, particularly in a region of star formation known for producing massive stars, is stellar feedback. This mechanism can elucidate the inside-out arrangement of events, which is not easily reproduced. For instance, we find that the correlations break down if we would arrange the clusters randomly and not by formation time, or if we use other reference points instead of the older clusters that are largely located at central locations (see randomized trials in Appendix B.5). Furthermore, by effectively accelerating nearby gas reservoirs, the feedback scenario accounts for the observation that the youngest clusters exhibit the highest velocities relative to the older, more massive clusters (Fig. 3). This scenario is already outlined for the four cluster chains, as discussed in [P23](#); [P25](#); or [MR25](#), which find acceleration from older to younger clusters, with the youngest moving away the fastest from the centre of Sco-Cen. The simplest scenario that aligns with these observations posits that feedback from prior episodes of star formation compresses and accelerates adjacent gas reservoirs of the primordial Sco-Cen gas cloud, ultimately leading to the formation of new stars (e.g., [de Avillez & Breitschwerdt 2005](#); [Großschedl et al. 2021](#); [P23](#); [P25](#); [Alves et al. 2025](#)). This mechanism essentially embodies the [Elmegreen & Lada \(1977\)](#) scenario in action, which naturally ends when the capacity to compress molecular gas into collapsing dense cores is exhausted.

The plateaus observed in the cumulative velocity dispersion (Fig. 1) warrant further investigation. These plateaus are not perfectly flat and exhibit, on average, subtle increases in velocity dispersion between the transitions. In this context, plateaus suggest the presence of a relatively coherent reservoir of gas forming a group of clusters, analogous to “peas in a pod” (see also Fig. 2). In this analogy, the jumps in σ_{3D} over time can be seen as star formation transitioning into a new “gas pod”, at slightly different average velocity, either primordial or, likely, affected by feedback. It remains to be studied how much of the next “pod” was created by fragmentation of the primordial gas cloud and how much of it was assembled by feedback from the previous star

formation episode. The CrA, LCC, and USco chains of clusters, representing the later stages of the formation of the association, clearly require a more dominant role for feedback, to be able to explain the observed accelerations ([P23](#); [P25](#); [MR25](#)). It seems reasonable to posit that the impact of feedback on the formation is not constant over the formation of an OB association, but coupled to the simultaneous presence of massive stars and their feedback output.

The three to four periods of enhanced star-formation rate found in the star formation history of Sco-Cen, as reported in [R23b](#)³, could be interpreted as observational evidence in support of the so-called “Type-I triggering”, discussed in [Dale et al. \(2015a\)](#). This type of star formation triggering, although posited to be theoretically unlikely, describes a temporal increase in the star formation rate, which is attributed to the presence of massive stars able to shape their environments, not unlike the scenario proposed above.

Looking at the cumulative Size in Fig. 1 (right panel), we find a general increasing trend of Sco-Cen’s extent. This behaviour might remind one of the time-size relation reported in [Efremov & Elmegreen \(1998](#), hereafter Ef&El98) (i.e., $t_{SF}(\text{Myr}) \sim S(\text{pc})^{0.5}$), see also [Elmegreen & Efremov \(1998\)](#). This is, however, a correlation where the timescale of star formation was plotted versus the size of a region, where the regions reach from dense cores, over clusters and OB associations, to whole complexes within spiral arms. This is not the same measurement, since we look at the stellar build-up of one OB association that is composed of clusters of different ages. Each of these clusters might have a similar star formation time scale from birth until all gas is removed, while Ef&El98 look into different hierarchical structures that are connected to star formation. Future work is needed to better understand such correlations and to fully uncover the spatial and temporal evolution of the stellar build-up in Sco-Cen.

5.1. Expansion of Sco-Cen

Using *Gaia* DR1, [Wright & Mamajek \(2018\)](#) found no evidence of expansion in Sco-Cen. With *Gaia* DR3, we revisit this question by examining the relative motions of the 32 Sco-Cen clusters. This updated view of Sco-Cen covers a larger area than previous studies (such as [Wright & Mamajek 2018](#)), which allows us, together with the higher precision of *Gaia* DR3, to reinvestigate the internal motions of the region. We find clear evidence for expansion, with a present-day speed of about 10 pc Myr^{-1} , which likely started around 11–14 Myr ago (Fig. 3–4, Table 1). Similar expansion patterns have been found for individual cluster chains ([P23](#); [P25](#); [MR25](#)), while we confirm expansion for the whole Sco-Cen region.

Additionally, we find that not only the speed but in particular the radial component of the motions shows a clear expansion of the whole region, similar to a Hubble flow (Fig. 4). These spatio-kinematic patterns in Sco-Cen, as presented in Figs. 2–4, are consistent with the hypothesis that the assembly of the Sco-Cen association happened sequentially and propagated from the inside out ([R23b](#)). The onset of expansion fits the age of the older clusters in Sco-Cen. Moreover, these older clusters are more massive and are the main source of stellar feedback in Sco-Cen; hence, they probably influenced the accumulation or even the momenta of the remaining clouds before they started to form

³ The youngest period of enhanced star formation is less pronounced in our work, since we excluded the two Chamaeleon clusters, which are part of [R23b](#).

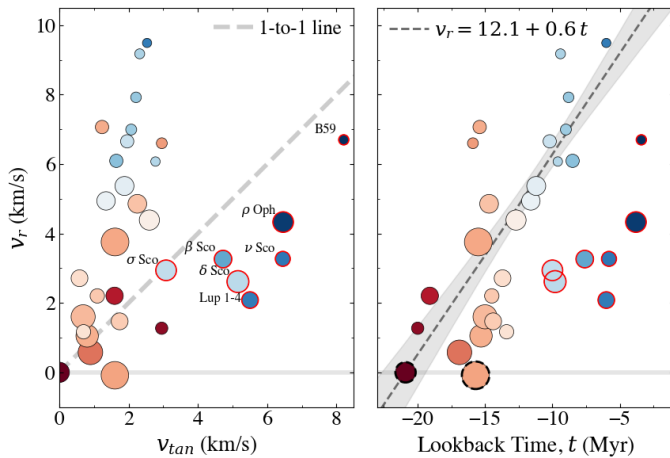


Fig. 6. Radial component of the relative cluster motions (v_r) versus the tangential component (v_{tan}) (left panel), and versus formation time (right panel), with e Lup as reference point. Symbols and colours are as in Fig. 3. The grey, dashed line in the left panel is a 1-to-1 line. The dark-grey, dashed line in the right panel shows a linear fit to data of 23 clusters, after removing the seven red-circled and the two black-dashed-circled clusters. The solid, light-grey line at $v_r = 0$, in both panels, marks the transition from radial outward (> 0) to inward (< 0) motion.

stars (e.g., Fuchs et al. 2006; Breitschwerdt et al. 2016; Krause et al. 2018; Großschedl et al. 2021)

Other mechanisms, like the relaxation due to gas dispersal and the general influence of Galactic dynamics, should also be taken into account (e.g., differential rotation or shear). We investigated the PV-diagrams in the three Galactic directions, XYZ (see Fig. 5 & Table 2). We find that the expansion patterns are largely comparable with each other within the uncertainties in the three dimensions. Especially when removing seven clusters with somewhat peculiar motions (see details in Sect. 5.2), we see almost isotropic expansion. If anything, there appears to be a slightly faster expansion in the X -direction when removing the seven odd clusters. Considering the effect of Galactic dynamics, one would rather expect a larger value in the Y -direction. This suggests that the Sco-Cen association is not (yet) strongly affected by Galactic dynamics and that we still observe the dynamics imprinted from the association’s formation history. A similar conclusion is presented in MR25, where no strong effects of Galactic dynamics are observed for the TWA cluster chain. Detailed modelling is warranted to disentangle the different influences.

5.2. Peculiar tangential motions of seven clusters

Figure 6 compares the radial component and the tangential component of the motions relative to e Lup (v_r vs v_{tan} , left panel). We see that for most clusters the radial component dominates over the tangential component, while older clusters tend to have generally lower relative velocities in both radial and tangential directions. The older clusters are largely located at central locations, similar to e Lup, and their formation was likely less influenced by feedback, since they are the source of most massive stars. Hence, the expansion pattern of the older clusters is more likely dominated by gas dispersal and dynamical relaxation, probably influenced by their internal feedback.

There are seven younger clusters (ages < 12 Myr), in and around USco, which also have a significant tangential component, concerning ρ Oph, ν Sco, δ Sco, β Sco, Lup 1-4, and also

B59. This is not completely unexpected, since massive stars exist in USco, and there is some evidence of additional forces in this region (e.g., Neuhäuser et al. 2020; Squicciarini et al. 2021; Miret-Roig et al. 2022b; Alves et al. 2025).

The right panel of Fig. 6 is similar to the speed–time relation in Fig. 3, while here only the radial component is plotted versus time. We find a similar increase in relative velocity with time, while there appear to be some outliers. These outliers are the same clusters that also have a significant tangential component, as marked by the red circles. We fit a linear regression to the data of 23 clusters, after removing the seven odd clusters, and the two clusters e Lup (reference point) and ν Cen. The latter is one of the most massive clusters in Sco-Cen and it shows here a minor negative value in v_r . The linear fit delivers a slope of $0.58 \pm 0.09 \text{ km s}^{-1} \text{ Myr}^{-1}$. This expansion speed is somewhat higher than the one from the speed–time relation (cf., $0.45 \pm 0.08 \text{ km s}^{-1} \text{ Myr}^{-1}$), while consistent within the uncertainties. An expansion between $5\text{--}7 \text{ km s}^{-1} \text{ Myr}^{-1}$ was also found for the individual cluster chains in P23; P25 or MR25. This highlights that the expansion is consistent in different directions of the association. The intercept in Fig. 6 delivers a velocity of about $12.1 \pm 1.1 \text{ km s}^{-1}$ ($12.3 \pm 1.2 \text{ pc Myr}^{-1}$), which could be interpreted as the present-day outward expansion speed of the association, when ignoring peculiar motions. This value is higher but consistent within the uncertainties when compared to the value delivered from the speed–time relation (cf., $10.8 \pm 0.9 \text{ pc Myr}^{-1}$, see Fig. 3 & Table 1).

As mentioned above (Sect. 4.2), we find that the seven clusters with peculiar tangential motions also appear to be outliers in the ZW PV-diagram in Fig. 5. If we remove these seven clusters, we see a cleaner linear trend in ZW for the remaining 25 clusters. Fitting linear regressions to the data in the three PV-diagrams using all 32 clusters delivers expansion velocities between about $0.04\text{--}0.07 \text{ km s}^{-1} \text{ pc}^{-1}$. When using only the 25 clusters, we get more consensus, with expansion velocities around $0.06 \text{ km s}^{-1} \text{ pc}^{-1}$ (Table 2), suggesting isotropic expansion.

The inverse of the slopes from the three PV-diagrams gives in most cases a time of about 15–18 Myr (especially when only using 25 clusters), which could be tentatively interpreted as the onset of expansion. This is slightly earlier than the time delivered by the radial expansion in Figs. 4 or B.3, which is about 11–14 Myr due to the somewhat higher expansion velocity. One reason could be that the radial-motion–distance relation depicts all outward motions relative to a rest frame, while the PV-diagrams are showing only the three selected directions of motion in XYZ. Regardless of the method, we see in all cases that the various estimated expansion velocities are generally in agreement with the age of Sco-Cen, where the oldest cluster has an age of about 21 Myr. Hence, the expansion has probably set in a few Myr after the first clusters have formed.

Taking a closer look at the ZW diagram in Fig. 5, we find that the seven odd clusters toward USco appear to be moving relatively “downward”; hence, they appear to be moving relatively faster toward the Galactic mid-plane compared to the older bulk clusters of Sco-Cen, while at the same time being at relatively high Z positions (see vertical grey, dashed line in Fig. 5). This could be an indication of Galactic dynamics, where the pull of the gravitational potential was able to reverse the motions of clusters at higher Galactic Z , which would imply that these clusters might have been at higher Z positions in the past. These relative motions are not observed for older clusters at similar Z positions. On the other hand, it could be a sign of a more complex formation history towards USco, Lupus, and Pipe (B59),

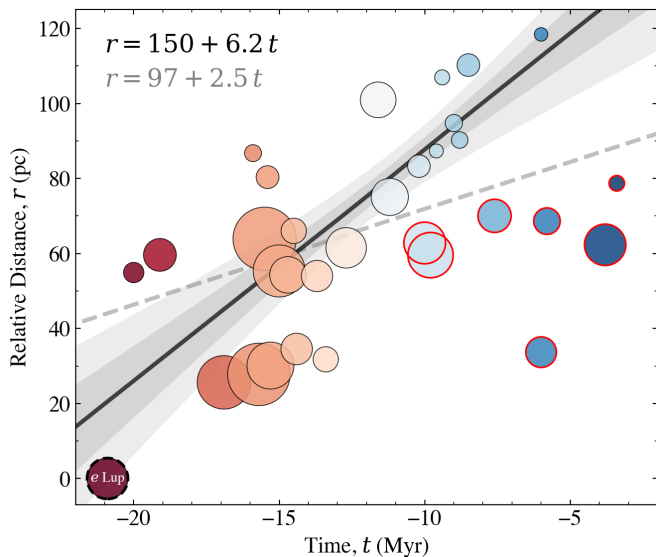


Fig. 7. Relative cluster distances versus formation time, with *e* Lup as reference point. Symbols and colours as in Fig. 3. Two linear relations are fitted, once for all clusters (dashed, light-grey line), and once for 25 clusters (solid, black line) after removing the seven, red-circled clusters; see also Fig. 6. The gray shaded areas show the 1-2- σ uncertainty ranges around the median slope when using 25 clusters.

which was also suggested in recent studies (e.g., Miret-Roig et al. 2022b; P25; Alves et al. 2025). Moreover, when considering the other two clusters toward the Pipe nebula (Pipe-North and θ Oph), we find that they also appear to be standing out by having somewhat higher relative motions when compared to the rest of the older clusters with ages > 15 Myr. A more detailed analysis of the peculiar motions in these regions is part of future work (e.g., S. Hutschenreuter et al., subm. to A&A).

5.3. Radial propagation speed of star formation

Looking at the relations in Figs. 3 and 4, we find that we can combine the resulting linear relations from the speed-time (dv/dt) and radial-motion-distance (dv_r/dr) relations, to determine the radial propagation speed of star formation (dr/dt). In this case, we are ignoring that we first have the speed (v) and second only the radial component of the motions (v_r); then we can write:

$$\frac{dr}{dt} \approx \frac{dv/dt}{dv_r/dr} \approx \frac{0.45 \text{ (km/s)/Myr}}{0.09 \text{ (km/s)/pc}} \approx 4.9 \frac{\text{pc}}{\text{Myr}} \approx 4.8 \frac{\text{km}}{\text{s}} \quad (6)$$

When using instead the dv_r/dr relation from Fig. 6 (right panel), then we can compare the same quantities; we get:

$$\frac{dr}{dt} = \frac{dv_r/dr}{dv_r/dr} = \frac{0.58 \text{ (km/s)/Myr}}{0.09 \text{ (km/s)/pc}} \approx 6.3 \frac{\text{pc}}{\text{Myr}} \approx 6.1 \frac{\text{km}}{\text{s}} \quad (7)$$

However, in the latter case, the seven odd clusters are not included in the value of dv_r/dr . Additionally, we directly plot the relative cluster distances versus time to get dr/dt , shown in Fig. 7. Again, we find that the seven odd clusters appear to be outliers, while the rest of the clusters follow a linear relation. When ignoring the odd clusters, we get a relation of about 6.2 pc Myr^{-1} (6.0 km s^{-1}), similar to Eq. (7).

We find that the radial propagation speed of star formation (assuming isotropic expansion) roughly matches or is higher than the total, present-day velocity dispersion of the entire system with $\sigma_{3D} \sim (4 \text{ to } 4.7) \text{ km/s}$. This implies that the system is

dominated by expansion, rather than random motions, and that it was initially dynamically cold.

5.4. Comparison to Larson's relation

Figure 1 shows that the stellar 3D velocity dispersion of Sco-Cen increased similarly as the spatial extent over the past 20 Myr. In Fig. 8, we investigate the relation of the cumulative σ_{3D} and S in log-space, which delivers the following correlation: $\sigma_{3D} \approx 0.14 \pm 0.03 S^{0.66 \pm 0.03}$. The exponent of about $0.66 \text{ km s}^{-1} \text{ pc}^{-1}$ is somewhat higher, but reminiscent of the canonical Larson's relation.

Larson (1981) reported that molecular clouds follow a velocity-dispersion-size relation of $\sigma_{3D} (\text{km s}^{-1}) = 1.1 S (\text{pc})^{0.38}$, with $\sigma_{3D} = \sqrt{3}\sigma$, as determined from observed CO linewidths, and S the projected cloud size (maximum linear dimension). Solomon et al. (1987) later found a steeper index of $\sigma (\text{km s}^{-1}) \approx S (\text{pc})^{0.5}$, a form that remains widely used (e.g., Heyer et al. 2009; Ballesteros-Paredes et al. 2011). This relation is often interpreted as a universal imprint of ISM turbulence (e.g., Heyer & Brunt 2004). Efremov & Elmegreen (1998) and Elmegreen & Efremov (1998) extended this picture by linking the linewidth-size relation ($\sigma \sim 0.7S^{0.5}$) to star formation timescales ($t_{SF} \sim S^{0.5}$), suggesting that star formation durations are comparable to turbulent crossing times and that the process is hierarchical and turbulence-driven. Our measurements differ in that we trace 3D stellar velocity dispersions after dynamical evolution, with “size” defined from the chronological build-up of clusters. Direct quantitative comparison is therefore not straightforward, and differences in slope and normalization are expected.

The correlation in Fig. 8 is challenging to construct, as data points are unevenly distributed and show plateaus and jumps (Fig. 1). Different methods for calculating cumulative σ_{3D} and size yield exponents in the range 0.3–1, underscoring systematic uncertainties. This prevents a definitive interpretation of whether our relation is directly comparable to Larson's relation.

Recent work on the expanding Cygnus OB association found consistency with Larson's relation and argued for a turbulent origin without the need for additional feedback (Quintana & Wright 2022). More generally, ISM turbulence may be driven by gravity, shear, converging flows, or stellar feedback (outflows, winds, radiation, supernovae), though the dominant mechanism remains debated (e.g., Krumholz & Burkhardt 2016; Padoan et al. 2016a,b, 2020; Ibáñez-Mejía et al. 2017; Seifried et al. 2018; Izquierdo et al. 2021).

If Larson's relation reflects turbulence, and if primordial cloud kinematics remain imprinted in Sco-Cen (e.g., Qian et al. 2012, 2018; Quintana & Wright 2022), one might expect the stellar motions to arise from turbulent processes and the hierarchical structure of the primordial cloud. However, our findings suggest otherwise: the increase in velocity dispersion and cluster speed is time-ordered and sequential, a structure difficult to reconcile with pure turbulence or a random occurrence of star formation progression. Randomized tests show that the observed relation between cluster age and velocity is reproduced only with very low probability, supporting a causal sequence more consistent with feedback-driven star formation.

Moreover, turbulence alone should generate a wide variety of kinematic states, whereas we observe systematic, step-wise changes in dispersion and speed that align with episodes of increased star formation. These transitions are better explained by a process capable of imparting ordered momentum, such as stel-

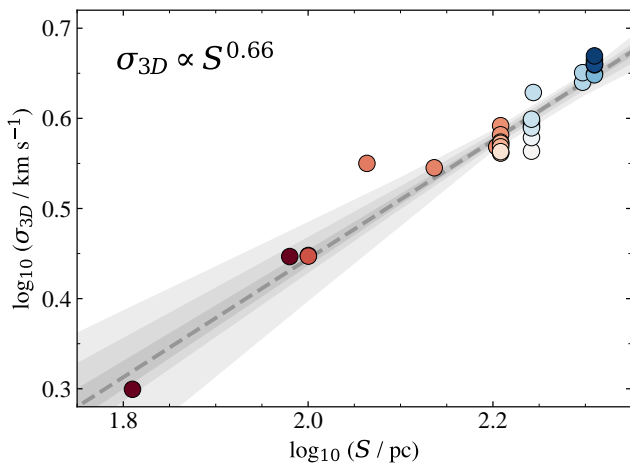


Fig. 8. Relation between cumulative 3D velocity dispersion (σ_{3D}) and cumulative size (S), plotted in log-space and colour-coded by formation time of the youngest included cluster, as in Fig. 1. The median slope is shown as a grey, dashed line, and the 1-2-3- σ uncertainty ranges as grey shaded areas.

lar feedback. While simulations indicate that large-scale turbulent modes can dominate stellar velocity structures, they also warn against using stellar kinematics as a direct tracer of cloud dynamics (e.g., Offner et al. 2009). Other studies point to feedback—particularly from supernovae—as a main driver of turbulence in Milky Way-like galaxies (e.g., Padoan et al. 2016a,b, 2017, 2020), suggesting that turbulence and feedback are not mutually exclusive but closely linked.

Finally, given these uncertainties, the similarity between Fig. 8 and Larson’s relation may be coincidental. While the scaling is suggestive, it should be interpreted with caution and clearly requires further investigation.

5.5. The importance of high resolution age maps

Our work underscores the importance of identifying the substructure and age distribution within a stellar association. When populations within an association are mixed, which is often unavoidable when studying more distant regions, the observed velocity dispersion may be misconstrued. Even Sco-Cen, the closest OB association to Earth, was traditionally divided into only three subgroups with three different ages (see Appendix A.1). Thanks to *Gaia*, we now know that Sco-Cen comprises more than 30 individual stellar populations, each with distinct motions and ages, and with relatively low internal velocity dispersions per cluster.

For example, Comeron et al. (1998) reported line-of-sight velocity dispersions of up to 60 km s^{-1} for the Cygnus superbubble and up to 15 km s^{-1} for the Canis Major OB1 association. They interpret these values as evidence for energetic expansion during the formation of these OB associations. Although this scenario is qualitatively consistent with our findings, we measure a significantly lower velocity dispersion for the entire Sco-Cen region, around 4 km s^{-1} . These relatively high velocity dispersions, reported by Comeron et al. (1998), could be real or could be due to various factors, such as the selection of radial velocities, instrumental limitations, or treatment of outliers and contamination. A likely contributor to the discrepancy is the presence of binary systems. In more distant clusters, the observed sample is typically dominated by massive stars, which are more

likely to be multiples, even with careful selection, and thus introduce additional dispersion in the measured velocities.

Regardless of the differences of the final, total values of σ_{3D} , we highlight in our work the importance of dissecting an association into stellar populations, with low velocity dispersions individually (of the order $1\text{--}2 \text{ km s}^{-1}$) and with different ages. This allows us to produce high-resolution age maps and study the evolution of velocity dispersion in detail (Fig. 2). We conclude that the relatively high velocity dispersion of an OB association is the product of mixing stellar populations within one region. Still, the discrepancy in the measured velocity dispersions needs more attention in future studies.

In conclusion, the presence of subpopulations and detailed age gradients found for the closest OB association to Earth should be considered when studying more distant regions or modelling the evolution of OB associations. Our results, along with those of others (e.g., Kerr et al. 2021; Chen et al. 2020; Hunt & Reffert 2023), indicate that OB associations should not be treated as a single stellar population (e.g., Brown et al. 1997), nor simply as a collection of a few subgroups (e.g., de Zeeuw et al. 1999), but rather as complex structures (e.g., Pecaut & Mamajek 2016; Wright & Mamajek 2018) composed of sequentially forming subpopulations (R23b; P25; MR25).

6. Summary & Conclusions

This study presents the first reconstruction of the time evolution of stellar velocity dispersion in a young OB association, using Sco-Cen as a case study. By combining high-precision *Gaia* DR3 astrometry with supplementary radial velocity measurements, we analysed the kinematics of 32 stellar clusters spanning ages from about 3 to 21 Myr.

We find a stepwise increase in the cumulative 3D velocity dispersion over time, together with a systematic inside-out build-up of the Sco-Cen association. These patterns support a structured, sequential formation scenario, in which feedback from massive stars originating from older clusters likely shaped the formation and early kinematics of younger populations. The observed jumps in velocity dispersion align with known bursts of star formation (approximately separated by 5 Myr), indicating that Sco-Cen assembled in phases from spatially and kinematically distinct gas reservoirs.

The motions of the Sco-Cen clusters reveal a well-defined expansion pattern, with a present-day rate of approximately $10\text{--}12 \text{ pc Myr}^{-1}$. The expansion likely began 11–13 Myr ago, as indicated by the outward motions, which are correlated with distance from the centre. The nearly isotropic velocity distribution suggests that internal dynamics and stellar feedback dominate over Galactic shear or differential rotation on the relevant timescales and spatial scales.

Our findings highlight the importance of high-resolution age maps and detailed kinematic substructure analysis in the study of OB associations. Simplistically treating these associations as single, homogeneous populations risks obscuring their complex formation pathways and underestimating their internal kinematic diversity. The sequential formation and expanding structure of Sco-Cen demonstrates the value of resolved, multi-epoch analyses for tracing the dynamical evolution and feedback processes in star-forming regions.

Acknowledgements. We thank the referee for constructive comments that improved the final version of this manuscript, and we thank Bruce Elmegreen for valuable comments on our analysis. JG acknowledges funding from the European Union, the Central Bohemian Region, and the Czech Academy of Sciences, as part of the MERIT fellowship (MSCA-COFUND Horizon Europe, Grant

agreement 101081195); the Collaborative Research Center 1601 (SFB 1601) funded by the Deutsche Forschungsgemeinschaft (DFG, 500700252); and the Austrian Research Promotion Agency (FFG, <https://www.ffg.at/>), project number 873708. SR acknowledges funding by the Federal Ministry Republic of Austria for Climate Action, Environment, Energy, Mobility, Innovation, and Technology (BMK, <https://www.bmk.gv.at/>) and FFG under project number FO999892674. SR performed this work as an SAO postdoctoral fellow and acknowledges the Smithsonian Institution for their support. Co-funded by the European Union (ERC, ISM-FLOW, 101055318). Views and opinions expressed are, however, those of the author(s) only and do not necessarily reflect those of the European Union or the European Research Council. Neither the European Union nor the granting authority can be held responsible for them. This work has made use of data from the European Space Agency (ESA) mission *Gaia* (<https://www.cosmos.esa.int/gaia>), processed by the *Gaia* Data Processing and Analysis Consortium (DPAC, <https://www.cosmos.esa.int/web/gaia/dpac/consortium>). Funding for the DPAC has been provided by national institutions, in particular, the institutions participating in the *Gaia* Multi-lateral Agreement. This work has made use of Python (<https://www.python.org>); Astropy (Astropy Collaboration et al. 2013, 2022); NumPy (van der Walt et al. 2011); Matplotlib (Hunter 2007); SciPy (Virtanen et al. 2020); Plotly (Plotly Technologies Inc. 2015); TOPCAT (Taylor 2005); and the VizieR catalog access tool (Ochsenbein et al. 2000), and Aladin sky atlas (Bonnarel et al. 2000; Boch & Fernique 2014) operated at CDS, Strasbourg Observatory, France.

Gagné, J., Roy-Loubier, O., Faherty, J. K., Doyon, R., & Malo, L. 2018a, *ApJ*, 860, 43
 Gaia Collaboration, Brown, A. G. A., Vallenari, A., et al. 2016, *A&A*, 595, A2
 Gaia Collaboration, Vallenari, A., Brown, A. G. A., et al. 2023, *A&A*, 674, A1
 Galli, P. A. B., Bertout, C., Teixeira, R., & Ducourant, C. 2013, *A&A*, 558, A77
 Gilmore, G., Randich, S., Asplund, M., et al. 2012, *The Messenger*, 147, 25
 Gontcharov, G. A. 2006, *Astronomy Letters*, 32, 759
 Großschedl, J. E., Alves, J., Meingast, S., & Herbst-Kiss, G. 2021, *A&A*, 647, A91
 Guenther, E. W., Esposito, M., Mundt, R., et al. 2007, *A&A*, 467, 1147
 Heyer, M., Krawczyk, C., Duval, J., & Jackson, J. M. 2009, *ApJ*, 699, 1092
 Heyer, M. H. & Brunt, C. M. 2004, *ApJ*, 615, L45
 Hunt, E. L. & Reffert, S. 2023, *A&A*, 673, A114
 Hunter, J. D. 2007, *Computing in Science and Engineering*, 9, 90
 Ibáñez-Mejía, J. C., Mac Low, M.-M., Klessen, R. S., & Baczynski, C. 2017, *ApJ*, 850, 62
 Izquierdo, A. F., Smith, R. J., Glover, S. C. O., et al. 2021, *MNRAS*, 500, 5268
 Jackson, R. J., Jeffries, R. D., Wright, N. J., et al. 2022, *MNRAS*, 509, 1664
 James, D. J., Melo, C., Santos, N. C., & Bouvier, J. 2006, *A&A*, 446, 971
 Jilinski, E., Daflon, S., Cunha, K., & de La Reza, R. 2006, *A&A*, 448, 1001
 Joergens, V. & Guenther, E. 2001, *A&A*, 379, L9
 Kamaya, H. 2004, *AJ*, 128, 761
 Katz, D., Sartoretti, P., Guerrier, A., et al. 2023, *A&A*, 674, A5
 Kerr, R. M. P., Rizzuto, A. C., Kraus, A. L., & Offner, S. S. R. 2021, *ApJ*, 917, 23
 Kos, J., Bland-Hawthorn, J., Asplund, M., et al. 2019, *A&A*, 631, A166
 Krause, M. G. H., Burkert, A., Diehl, R., et al. 2018, *A&A*, 619, A120
 Kroupa, P. 1995, *MNRAS*, 277, 1522
 Kroupa, P. 2008, in *The Cambridge N-Body Lectures*, ed. S. J. Aarseth, C. A. Tout, & R. A. Mardling, Vol. 760 (Springer Dordrecht), 181
 Krumholz, M. R. & Burkhardt, B. 2016, *MNRAS*, 458, 1671
 Kuhn, M. A., Hillenbrand, L. A., Sills, A., Feigelson, E. D., & Getman, K. V. 2019, *ApJ*, 870, 32
 Kunder, A., Kordopatis, G., Steinmetz, M., et al. 2017, *AJ*, 153, 75
 Lada, C. J. & Lada, E. A. 2003, *ARA&A*, 41, 57
 Lada, C. J., Margulis, M., & Dearborn, D. 1984, *ApJ*, 285, 141
 Larson, R. B. 1981, *MNRAS*, 194, 809
 Luhman, K. L. 2023, *AJ*, 165, 269
 Lynga, G. & Palous, J. 1987, *A&A*, 188, 35
 Majewski, S. R., Schiavon, R. P., Frinchaboy, P. M., et al. 2017, *AJ*, 154, 94
 Mamajek, E. E. & Feigelson, E. D. 2001, in *Astronomical Society of the Pacific Conference Series*, Vol. 244, *Young Stars Near Earth: Progress and Prospects*, ed. R. Jayawardhana & T. Greene, 104–115
 Miret-Roig, N., Alves, J., Ratzenböck, S., et al. 2025, *A&A*, 694, A60
 Miret-Roig, N., Galli, P. A. B., Olivares, J., et al. 2022b, *A&A*, 667, A163
 Murphy, S. J., Lawson, W. A., & Bessell, M. S. 2013, *MNRAS*, 435, 1325
 Neuhäuser, R., Gießler, F., & Hambaryan, V. V. 2020, *MNRAS*, 498, 899
 Nguyen, D. C., Brandeker, A., van Kerkwijk, M. H., & Jayawardhana, R. 2012, *ApJ*, 745, 119
 Ochsenbein, F., Bauer, P., & Marcout, J. 2000, *A&AS*, 143, 23
 Offner, S. S. R., Hansen, C. E., & Krumholz, M. R. 2009, *ApJ*, 704, L124
 Padoan, P., Haugbølle, T., Nordlund, Å., & Frimann, S. 2017, *ApJ*, 840, 48
 Padoan, P., Juvela, M., Pan, L., Haugbølle, T., & Nordlund, Å. 2016b, *ApJ*, 826, 140
 Padoan, P., Pan, L., Haugbølle, T., & Nordlund, Å. 2016a, *ApJ*, 822, 11
 Padoan, P., Pan, L., Juvela, M., Haugbølle, T., & Nordlund, Å. 2020, *ApJ*, 900, 82
 Pearson, K. 1895, *Proceedings of the Royal Society of London Series I*, 58, 240
 Pecaut, M. J. & Mamajek, E. E. 2016, *MNRAS*, 461, 794
 Plotly Technologies Inc. 2015, *Collaborative data science*, Montreal, QC
 Poleski, R. 2013, arXiv e-prints, arXiv:1306.2945
 Posch, L., Alves, J., Miret-Roig, N., et al. 2025, *A&A*, 693, A175
 Posch, L., Miret-Roig, N., Alves, J., et al. 2023, *A&A*, 679, L10
 Preibisch, T. & Mamajek, E. 2008, in *Handbook of Star Forming Regions*, Volume II, ed. B. Reipurth, Vol. 5 (Astronomical Society of the Pacific), 235
 Preibisch, T. & Zinnecker, H. 1999, *AJ*, 117, 2381
 Qian, L., Li, D., Gao, Y., Xu, H., & Pan, Z. 2018, *ApJ*, 864, 116
 Qian, L., Li, D., & Goldsmith, P. F. 2012, *ApJ*, 760, 147
 Quintana, A. L. & Wright, N. J. 2022, *MNRAS*, 515, 687
 Ratzenböck, S., Großschedl, J. E., Alves, J., et al. 2023b, *A&A*, 678, A71
 Ratzenböck, S., Großschedl, J. E., Möller, T., et al. 2023a, *A&A*, 677, A59
 Sacco, G. G., Spina, L., Randich, S., et al. 2017, *A&A*, 601, A97
 Santana, F. A., Beaton, R. L., Covey, K. R., et al. 2021, *AJ*, 162, 303
 Schönrich, R., Binney, J., & Dehnen, W. 2010, *MNRAS*, 403, 1829
 Seifried, D., Walch, S., Haid, S., Girichidis, P., & Naab, T. 2018, *ApJ*, 855, 81
 Slesnick, C. L., Hillenbrand, L. A., & Carpenter, J. M. 2008, *ApJ*, 688, 377
 Solomon, P. M., Rivolo, A. R., Barrett, J., & Yahil, A. 1987, *ApJ*, 319, 730
 Spearman, C. 1904, *The American Journal of Psychology*, 15, 72
 Squicciarini, V., Gratton, R., Bonavita, M., & Mesa, D. 2021, *MNRAS*, 507, 1381

Steinmetz, M., Matijević, G., Enke, H., et al. 2020a, AJ, 160, 82

Swiggum, C., Alves, J., Benjamin, R., et al. 2024, Nature, 631, 49

Swiggum, C., Alves, J., & D'Onghia, E. 2025, arXiv e-prints, arXiv:2504.02825

Taylor, M. B. 2005, in Astronomical Society of the Pacific Conference Series, Vol. 347, Astronomical Data Analysis Software and Systems XIV, ed. P. Shopbell, M. Britton, & R. Ebert, 29

Torres, C. A. O., Quast, G. R., da Silva, L., et al. 2006, A&A, 460, 695

Tsantaki, M., Pancino, E., Marrese, P., et al. 2022, A&A, 659, A95

van der Walt, S., Colbert, S. C., & Varoquaux, G. 2011, Computing in Science and Engineering, 13, 22

Virtanen, P., Gommers, R., Oliphant, T. E., et al. 2020, Nature Methods, 17, 261

Wichmann, R., Covino, E., Alcalá, J. M., et al. 1999, MNRAS, 307, 909

Wright, N. J., Kounkel, M., Zari, E., Goodwin, S., & Jeffries, R. D. 2023, in Astronomical Society of the Pacific Conference Series, Vol. 534, Astronomical Society of the Pacific Conference Series, ed. S. Inutsuka, Y. Aikawa, T. Muto, K. Tomida, & M. Tamura, 129

Wright, N. J. & Mamajek, E. E. 2018, MNRAS, 476, 381

Appendix A: Used data and parameters

A.1. The Sco-Cen cluster sample

As in R23b, we consider only 34 out of the total 37 SigMA selected clusters from R23a as probable members of the Sco-Cen association⁴. The 34 clusters contain a total of 12,972 stellar members. An overview is given in Table A.2, where we list the cluster names, ages, and number statistics. Moreover, each cluster is assigned to a traditional region (TR), as defined in 2D projection. The TRs include the classical Blaauw (1946) regions Upper-Scorpius (US), Upper Centaurus Lupus (UCL), and Lower Centaurus Crux (LCC), which have often been treated as the three stellar sub-groups of Sco-Cen (e.g., de Zeeuw et al. 1999; Mamajek & Feigelson 2001; Preibisch & Mamajek 2008). R23a included clusters toward Pipe, Corona Australis (CrA), and Chamaeleon (Cham), and to the Galactic North-East (NE) of Sco-Cen. The two clusters in the TW Hydriæ association (TWA-a, TWA-b) were added to Sco-Cen by MR25, while stellar members were previously reported in Gagné et al. (2018a) or Luhman (2023). The 36 clusters contain a total of 13,011 stellar members.

In our analysis, we do not include the Chamaeleon clusters (Cham-I, Cham-II, Cen-Far), since these are connected to a background structure, as discussed in Edenhofer et al. (2024b). The authors identified a “C” structure in a 3D dust map (Edenhofer et al. 2024a). The shell-like structure was likely created by a supernova, creating a rim that contains the Chameleon, Musca, and Coalsack clouds, located at the back of the main Sco-Cen complex. The history of this structure is likely connected to Sco-Cen, where remaining gas was possibly influenced by massive stellar feedback originating from the OB association. Nevertheless, we remove the clusters that are associated with the “C” structure from our current analysis, since the relative motions show peculiarities compared to the rest of the Sco-Cen clusters, and they are also located slightly detached from the main body of Sco-Cen. Moreover, we do not include the cluster μ Sco in our analysis, since it has poor RV statistics; only two stellar members pass our RV quality criteria (Appendix A.4), which additionally show a large dispersion in RV space.

We combine the SigMA Sco-Cen sample with the TWA sample (66 stellar members). We find that 27 sources are in common, which are candidate members of σ Cen, a cluster which is connected to TWA in a cluster chain. The overlapping sources have low statistical stability for σ Cen, as given by the SigMA algorithm, and they are scattered suspiciously in front of the cluster along the line-of-sight, which makes it more likely that these sources belong to TWA (see also MR25). Hence, these 27 sources are counted to TWA from here on. TWA was tentatively split into two clusters in MR25, named TWA-a and TWA-b, containing 44 and 22 stellar members, respectively.

Eventually, we analyse 32 Sco-Cen clusters in this paper that contain a total of 12,612 stellar members, with 12,546 retrieved from the 30 SigMA Sco-Cen clusters (R23a) and 66 from the two TWA clusters (MR25). For completeness, we also report statistics for the four removed SigMA clusters in Table A.2.

A.2. Parameters and parameter transformations

We use the astrometric parameters from *Gaia* DR3 and supplementary radial velocity data:

– α, δ (deg): Right ascension and Declination

⁴ Three clusters are likely unrelated: Norma-North, Oph-SE, and Oph-NF (see R23b).

- l, b (deg): Galactic longitude and latitude
- ϖ (mas): parallax $\Rightarrow d$ (pc): distance ($1/\varpi$)
- μ_α, μ_δ (mas yr⁻¹): proper motions along α and δ (for simplicity we denote here $\mu_\alpha \cos(\delta)$ as μ_α)
- μ_l, μ_b (mas yr⁻¹): proper motions along l and b (for simplicity we denote here $\mu_l \cos(b)$ as μ_l)
- v_{RV} (km s⁻¹): Heliocentric radial velocity (line-of-sight motion relative to the Sun, determined from spectra)

In this work, we use the inverse of the parallax as a distance estimate, which is reasonable for targets within about 200 pc from the Sun and for sources with low uncertainties (see R23a).

The velocities are corrected for the standard solar motion (Schönrich et al. 2010), hence transformed to velocities relative to the local standard of rest (LSR) with the help of `astropy.coordinates` (Astropy Collaboration et al. 2013, 2018, 2022). They are given as $\mu_{\alpha,\text{lsr}}$, $\mu_{\delta,\text{lsr}}$, $\mu_{l,\text{lsr}}$, $\mu_{b,\text{lsr}}$ (mas/yr) and $v_{\text{RV},\text{lsr}}$ (km/s). The transformation from μ_x to $\mu_{x,\text{lsr}}$ can alternatively be achieved by the transformations outlined in Poleski (2013). The tangential velocities (v_α , v_δ , v_l , v_b , or $v_{\alpha,\text{lsr}}$, $v_{\delta,\text{lsr}}$, $v_{l,\text{lsr}}$, $v_{b,\text{lsr}}$) are derived from proper motions and parallaxes as follows:

$$v_x \text{ (km s}^{-1}\text{)} = 4.74047 \cdot \mu_x / \varpi \quad (\text{A.1})$$

The proper motion can be entered heliocentric or LSR-corrected in the above formula, while the latter results in tangential velocities in the LSR frame. XYZ are the Heliocentric Galactic Cartesian coordinates in parsec (pc):

$$X = d \cos(l) \cos(b), \quad Y = d \sin(l) \cos(b), \quad Z = d \sin(b) \quad (\text{A.2})$$

X is positive toward the Galactic centre, Y is positive in the direction of Galactic rotation, and Z is positive toward the Galactic North Pole. The corresponding Heliocentric Galactic Cartesian velocities in the directions of XYZ are given as UVW (in km s⁻¹):

$$\begin{aligned} U &= v_{\text{RV}} \cos(l) \cos(b) - v_l \sin(l) - v_b \cos(l) \sin(b) \\ V &= v_{\text{RV}} \sin(l) \cos(b) + v_l \cos(l) - v_b \sin(l) \sin(b) \\ W &= v_{\text{RV}} \sin(b) + v_b \cos(b) \end{aligned} \quad (\text{A.3})$$

When substituting the given velocities with $v_{\text{RV},\text{lsr}}$, $v_{l,\text{lsr}}$, and $v_{b,\text{lsr}}$, we get the Cartesian velocities relative to the local standard of rest (LSR), denoted as U_{LSR} , V_{LSR} , and W_{LSR} (km s⁻¹). Alternatively, UVW_{LSR} is calculated from UVW by adding the values of the standard Solar motion from Schönrich et al. (2010). In our analysis, one can use both the Heliocentric or LSR corrected Galactic Cartesian velocities, since it does not make a difference when investigating relative motions within a region.

To get uncertainties for the derived parameters, we use an error sampling approach. We sample from the various parameters by randomly drawing from Gaussians, using the measurements and their uncertainties as the mean and standard deviation. For instance, to get the uncertainties of the tangential velocities, we use Eq. (A.1) and we sample over the parallaxes and proper motions, and their uncertainties. We then use the median and standard deviation as the derived parameters and their uncertainties.

A.3. The radial velocity surveys

Table A.1 lists 22 radial velocity surveys or literature studies that are combined in this work to get more complete 6D phase space information per cluster. The RV surveys are combined with the *Gaia* DR3 catalogue (13 011 sources) by using the source IDs or sky cross-matches. A *Gaia source_id* match is possible for

catalogues that contain information on *Gaia*, 2MASS, or HIP IDs, which can be matched within the *Gaia* archive (see also Appendix A in R23a). For other catalogues, we use a 1" cross-match radius, using the closest match.

The list in Table A.1 includes several well-known large-scale surveys and also smaller-scale spectroscopic studies. This creates a heterogeneous RV sample, observed with different instruments at different resolutions, and processed with different pipelines. Hence, we are dealing with variable data coverage and possible systematic differences between the RV measurements. Moreover, the measurement uncertainties could have additional systematics and might have been estimated differently, further complicating a comparison at face value. One way forward could be to use an already homogenized catalogue, like the Survey of Surveys (SoS) by Tsantaki et al. (2022), which is a compilation of six spectroscopic surveys (*Gaia* DR2, APOGEE DR16, GALAH DR2, *Gaia*-ESO DR3, LAMOST DR5, RAVE DR6). However, most of the data releases (DR) of the included surveys have already been superseded by more recent releases. Hence, we decided to use the most recent DRs and other original literature data, which were not used by SoS.

Small systematic variations between surveys are not highly critical when averaging the motions per cluster to get each cluster's median or mean motion, while for the calculation of the velocity dispersion, we aim at higher quality. Hence, we apply quality criteria, outlined in Appendix A.4, and we compare the individually measured RVs to each other to identify possible systematic shifts between the surveys (for this, we matched the full external catalogues with *Gaia* DR3). Binaries could also cause discrepancies between measurements from different surveys, however, we would not expect a systematic shift in one direction between two surveys. We use *Gaia* DR3 RVs as zero-point, since this is the largest survey in our list, covering the whole sky; hence, we can compare it to the full available catalogues of the other surveys. We only identify significant global shifts in four cases: APOGEE2, GALAH, RAVE, and PCRV. For the rest of the surveys, we either do not find a significant shift or there are not enough sources in common to identify a clear trend. The average shifts are given in Table A.1 as ΔRV . We do not correct for these shifts, since we did not test for dependencies (relative to T_{eff} , $\log g$, or metallicity; see, e.g., Tsantaki et al. 2022), which would go beyond the scope of this paper. To account for this additional uncertainty, we add the shift quadratically to the measurement uncertainties of these four surveys. Concerning the measurement uncertainties in general, we do not consider any systematics between the surveys, and we use the reported RV uncertainties (e_{RV}) for simplicity, and we correct them only in the four mentioned cases (i.e., $e_{\text{RV,corr}} = \sqrt{e_{\text{RV}}^2 + \Delta RV^2}$).

A.4. Quality criteria

We use the stability criterion per stellar cluster member that is provided in the SigMA catalogue (R23a). This criterion indicates how often individual sources appear throughout the ensemble of clustering solutions per cluster, denoted as stability in the range from 0–100%; hence, sources with low stability are less reliable cluster members. The maximum stability per cluster is variable, while generally higher for richer clusters, since they have been more often retained by SigMA. Hence, we apply a variable stability cut per cluster, which is set as follows. R23a find that stars in more “stable” clusters (generally the richer and more massive ones) have generally higher stability values ($\gtrsim 80\%$). R23a suggest that a cut at about $\text{stability} > 11\%$ would be

a reasonable discriminator for such clusters to select more reliable stellar cluster members. We decide to create a variable stability cut to account for the fact that the stability values of stars within sparser clusters are generally lower. First, we calculate the median stability per cluster, and then we use 10% of the median as the threshold, which gives less conservative values than the suggested 11%. The resulting value is used as the individual stability threshold per cluster: $\text{stab_threshold} = \text{median_stability} (\text{per cluster}) \cdot 0.1$. This value is listed in Table A.2 (Col. 5). We then only keep stars with: $\text{stability} > \text{stab_threshold}$. This procedure gives lower stability thresholds than 11% for all clusters, which ensures that we only remove the most obvious outliers, which is in particular critical for the less prominent clusters. This variable stability cut is applied both on the positional and the velocity data, while the latter requires additional quality checks for the RV data, as follows.

The sample size of the 3D velocity data (UVW) strongly depends on the available RV data (Table A.1). We find that about 50% of the sources (6529/13 011) have been targeted by at least one RV survey. Considering these sources, there are about 34% that have been targeted by more than one survey (2194/6529). This sample can be used to identify binary candidates. Additionally, we investigate the *Gaia* DR3 RUWE parameter (Castro-Ginard et al. 2024) that indicates if a source is a probable binary or multiple stellar system, further discussed in Appendix B.1.

To get a clean sample of RVs per cluster and at the same time retain significant numbers of sources, we apply the following quality criteria. In a first step, we retain only sources with low RV uncertainties, using a cut at $e_{\text{RV}} < 3.1 \text{ km s}^{-1}$. We decided on a relatively non-conservative cut to ensure that clusters with few RV measurements contain significant numbers of sources with RV information.

For sources observed by APOGEE2, we use the provided scatter parameter (VSCATTER), which is available if a source has been observed more than once within APOGEE2. We add the VSCATTER parameter to the APOGEE2 RV errors (VERR) as follows: $\text{VERR}_{\text{corr}} = \sqrt{\text{VERR}^2 + \text{VSCATTER}^2 + \Delta RV^2}$. ΔRV is the global shift between *Gaia* and APOGEE RVs that we have identified in the previous section. Using the corrected RV errors, sources with larger scatter (potential binary candidates) get automatically removed when applying the error cut from above. Sources without VSCATTER information, which were observed only once by APOGEE2, lack this information, and their errors might be underestimated. At this stage, we can not know about any additional scatter for such sources (if only observed once).

For sources with multiple observations from different surveys, we first calculate the weighted mean and weighted standard deviation as follows:

$$\bar{v}_{\text{RV}_w} = \frac{\sum w_i v_{\text{RV}_i}}{\sum w_i},$$

$$e_{\text{RV}_w} = \sqrt{\frac{\sum w_i (v_{\text{RV}_i} - \bar{v}_{\text{RV}_w})^2}{\sum w_i} \cdot \frac{N}{N-1}}, \quad (\text{A.4})$$

where $w_i = 1/e_{\text{RV}_i}^2$ are the weights. For our analysis, if a source was observed multiple times, we are using the RV measurement from the survey with the lowest error ($v_{\text{RV}_\text{best}}$). The weighted mean and standard deviation are used to test for significant deviations between the surveys, to remove potential binary or multiple candidates (similar to the scatter in APOGEE2). We keep sources with $|v_{\text{RV}_\text{best}} - \bar{v}_{\text{RV}_w}| < 3 \text{ km s}^{-1}$ and $e_{\text{RV}_w} < 3.1 \text{ km s}^{-1}$. We decided for this cut to be comparable to the used RV error cut introduced above.

Table A.1. Data references for radial velocities.

Ref.	References	Region	Survey Name / Notes / Comments	Number of sources			
				All	Matched	Used	ΔRV
1	Gaia Collaboration et al. (2023) , Katz et al. (2023)	All-Sky	Gaia DR3	33,812,183	4919 (3230)	2298 (919)	0
2	Majewski et al. (2017) , Santana et al. (2021) , Abdurro'uf et al. (2022)	USco, sub-parts of Sco-Cen	APOGEE2 SDSS DR17	722,905	1190 (341)	1021 (285)	-0.28
3	De Silva et al. (2015) ; Buder et al. (2021, 2024)	Parts of Southern Hemisphere	GALAH DR4 (Galactic Archaeology with HERMES)	906,661	1900 (529)	1529 (387)	-0.22
4	Gilmore et al. (2012) , Sacco et al. (2017) , Jackson et al. (2022)	Targeted clusters	Gaia-ESO iDR6 (GES)	107,779	125 (29)	112 (27)	0
5	Kunder et al. (2017) , Steinmetz et al. (2020a)	Southern Hemisphere	RAVE DR6 (The Radial Velocity Experiment)	451,636	135 (9)	105 (2)	0.34
6	Gontcharov (2006)	All-Sky	PCRV (Pulkovo Compilation of Radial Velocities) for 35,495 Hipparcos stars, standard stars compiled from other literature, homogenized RVs	35,495	111 (48)	60 (20)	0.1
7	Torres et al. (2006)	Southern Hemisphere	SACY (Search for associations containing young stars), 1511 observed by them, 115 from other literature	1626	241 (29)	208 (22)	0
8	Jilinski et al. (2006)	Sco-Cen	B-stars in Sco-Cen	119	25 (10)	14 (6)	0
9	Chen et al. (2011)	Sco-Cen	Magellan MIKE and Spitzer MIPS Study	192	91 (11)	74 (7)	0
10	Dahm et al. (2012)	USco	HIRES for 50 members, MIKE for 44 members	131	79 (10)	67 (10)	0
11	Miret-Roig et al. (2022b)	USco	Compilation of observed and archival spectra, R~20,000–115,000	157	154 (9)	123 (4)	0
12	Fang et al. (2023)	USco	Collected from Keck/HIRES Optical Survey, R~34,000, typical RV-uncertainty ~ 1.4 km/s	115	97 (5)	90 (3)	0
13	James et al. (2006)	Cham, Lup, CrA	ESO/FEROS, R~32,000	53	22 (0)	20 (0)	0
14	Guenther et al. (2007)	Cham, Lup, CrA, Oph	ESO/FEROS, R~48,000	96	39 (1)	32 (1)	0
15	Wichmann et al. (1999)	Lupus	ROSAT-discovered WTTS near Lupus	71	45 (2)	34 (2)	0
16	Galli et al. (2013)	Lupus, Oph	Kinematic study of the Lupus star-forming region	52	42 (4)	42 (4)	0
17	Joergens & Guenther (2001)	Cham I	UVES spectra at 6000–10,400 Å (R~40,000)	12	11 (5)	11 (5)	0
18	Nguyen et al. (2012)	Cham I	MIKE spectra at 4800–9400 Å (R~60,000)	67	46 (4)	43 (4)	0
19	Biazzo et al. (2012)	Cham II	UVES/GIRAFFE	83	29 (22)	19 (16)	0
20	Murphy et al. (2013)	eps Cham	WiFeS multi-epoch spectroscopy, R~7000	45	20 (9)	20 (9)	0
21	Luhman (2023)	TWA	Literature compilation from 16 references (we excluded <i>Gaia</i> DR3 and GALAH DR2)	38	37 (16)	21 (14)	0
22	Miret-Roig et al. (2025)	TWA	Archival compilation of spectra from ESO, CFHT, and NOIRLab, named RV _{ispec}	24	24 (2)	14 (2)	0

Notes. The first seven references are large spectroscopic survey programs or RV compilations, partially covering the whole sky or a full hemisphere. The rest are targeted observations collected from the mentioned literature, loosely grouped by observed region. Col. 5 lists the total number of sources available in each survey. Col. 6 & 7 list the number of sources matched with the Sco-Cen sample and the number of used RVs; in brackets, we give the number of sources that only have an RV measurement from this survey but not in any of the other surveys. Col. 8 gives the global RV shift between the given survey and *Gaia* DR3 RVs, if identified.

After these applied cuts, there are still some RVs per cluster that are clearly scattered beyond their median velocities. Significant deviations in the motions of single stars from the bulk motion of the parent cluster could have several reasons, such as unresolved binaries, mismatches, or contamination from unrelated stellar populations or field stars. To clean the RV sample per cluster, we exclude potential contaminants or outliers first via a global outlier cut and second via sigma clipping. We use the LSR corrected RVs ($v_{\text{RV},\text{lsr}}$); they show less scatter, since artificial trends are removed that appear when using the heliocentric RVs. First, we find that sources scattered beyond $-2.5 \leq v_{\text{RV},\text{lsr}} (\text{km s}^{-1}) \leq 18.0$ are general outliers when considering the RV distribution of the whole Sco-Cen association, and we globally remove sources beyond these boundaries. Next, we remove outliers with significant deviations from the bulk motion of each cluster by applying sigma clipping at 3σ around each cluster's median- $v_{\text{RV},\text{lsr}}$. In most cases, this additional step removes only a few outliers or none.

Finally, the combined quality criteria, including the stability cut, the error cuts, removal of binary candidates, and sigma-clipping, leave 3222 (25%) sources out of 13,011. The individual numbers and fractions per cluster are given in Table A.2.

We compare the weighted mean with the finally selected *best* RVs per source (when observed multiple times) after applying the mentioned quality criteria. We do not find a significant deviation for the majority of these sources: $\text{MEDIAN}(v_{\text{RV},\text{best}} - \bar{v}_{\text{RV},\text{w}}) = (0.003^{+0.134}_{-0.162}) \text{ km/s.}$, underlining the robustness of these selected RV values.

Appendix B: Detailed methods descriptions

B.1. Calculating the cumulative velocity dispersion

Here, we give more details on the construction of Fig. 1, which shows the change of the cumulative 3D velocity dispersion with cluster formation time (or cluster age). The cumulative σ_{3D} is calculated chronologically by incorporating the stellar members of the clusters that lie within a certain time threshold. In more detail, we start to calculate σ_{3D} by using the stellar members of the oldest cluster, *e* Lup, and then add chronologically at each time step the stars of the next youngest cluster, until we reach the final time step that contains all stars in Sco-Cen, from old to young. At each time step, we calculate the total velocity dispersion of the stellar members that formed before the time threshold

Table A.2. Overview of 36 stellar clusters toward Sco-Cen from [R23a](#) (SigMA selected clusters) and [MR25](#) (TWA clusters), including radial velocity data statistics, sorted by cluster age.

Idx	SigMA	TR	Name	Stab.	Age (Myr)	Number of sources			
						XYZ _{all}	XYZ _{used} (%)	UVW _{all} (%)	UVW _{used} (%)
1	17	UCL	<i>e</i> Lup		8.2	20.9 ^{+0.7} _{-0.8}	516	468 (90.7)	199 (38.6)
2	12	UCL	Libra-South		3.9	20.0 ^{+2.5} _{-2.2}	71	65 (91.5)	26 (36.6)
3	9	US	US-foreground		4.6	19.1 ^{+2.4} _{-1.3}	276	254 (92.0)	173 (62.7)
4	15	UCL	ϕ Lup		6.8	16.9 ^{+0.9} _{-0.6}	1114	1047 (94.0)	514 (46.1)
5	27	Pipe	Pipe-North		1.9	15.9 ^{+1.6} _{-2.1}	42	40 (95.2)	21 (50.0)
6	20	UCL	ν Cen		7.8	15.7 ^{+0.3} _{-0.9}	1737	1522 (87.6)	709 (40.8)
7	21	LCC	σ Cen		9.3	15.5 ^{+0.6} _{-0.5}	1778	1618 (91.0)	881 (49.6)
8	28	Pipe	θ Oph		8.8	15.4 ^{+0.8} _{-1.9}	98	90 (91.8)	40 (40.8)
9	14	UCL	η Lup		6.4	15.3 ^{+0.6} _{-0.3}	769	722 (93.9)	386 (50.2)
10	10	UCL	V1062-Sco		9.9	15.0 ^{+0.9} _{-1.4}	1029	963 (93.6)	339 (32.9)
11	8	US	Scorpio-Body		5.7	14.7 ^{+0.8} _{-0.7}	373	344 (92.2)	147 (39.4)
12	31	CrA	Scorpio-Sting		1.6	14.5 ^{+0.6} _{-0.6}	132	129 (97.7)	42 (31.8)
13	19	UCL	ρ Lup		8.6	14.4 ^{+0.4} _{-0.9}	246	235 (95.5)	101 (41.1)
14	7	US	ρ Sco		7.3	13.7 ^{+1.3} _{-0.6}	240	227 (94.6)	132 (55.0)
15	18	UCL	UPK606		8.7	13.4 ^{+1.4} _{-0.7}	131	115 (87.8)	60 (45.8)
16	6	US	Antares		9.7	12.7 ^{+0.4} _{-1.7}	502	468 (93.2)	316 (62.9)
17	30	CrA	CrA-North		9.9	11.6 ^{+0.5} _{-0.8}	351	333 (94.9)	143 (40.7)
18	22	LCC	Acrux		9.9	11.2 ^{+1.0} _{-1.0}	394	385 (97.7)	222 (56.3)
19	23	LCC	Musca-foreground		9.9	10.2 ^{+1.0} _{-0.7}	95	88 (92.6)	46 (48.4)
20	5	US	σ Sco*		9.7	10.0 ^{+1.0} _{-0.5}	544	508 (93.4)	317 (58.3)
21	3	US	δ Sco*		9.9	9.8 ^{+1.2} _{-1.4}	691	674 (97.5)	512 (74.1)
22	35	NE	L134/L183		1.0	9.6 ^{+1.7} _{-2.2}	24	24 (100.0)	8 (33.3)
23	25	LCC	η Cham		7.8	9.4 ^{+1.4} _{-0.9}	30	23 (76.7)	15 (50.0)
24	–	TWA	TWA-a		9.9	9.0 ^{+2.0} _{-1.0}	44	44 (100.0)	36 (81.8)
25	24	LCC	ϵ Cham		9.9	8.8 ^{+0.6} _{-0.4}	39	36 (92.3)	32 (82.1)
26	29	CrA	CrA-Main		9.9	8.5 ^{+2.0} _{-2.4}	96	85 (88.5)	72 (75.0)
27	4	US	β Sco*		9.8	7.6 ^{+0.8} _{-0.7}	285	263 (92.3)	206 (72.3)
28	–	TWA	TWA-b		9.9	6.0 ^{+2.0} _{-1.0}	22	22 (100.0)	22 (100.0)
29	13	UCL	Lupus 1-4*		7.7	6.0 ^{+0.6} _{-0.9}	226	199 (88.1)	113 (50.0)
30	2	US	ν Sco*		10.0	5.8 ^{+1.8} _{-0.5}	150	147 (98.0)	118 (78.7)
31	1	US	ρ Oph/L1688*		9.9	3.8 ^{+0.4} _{-0.4}	535	507 (94.8)	346 (64.7)
32	26	Pipe	B59*		4.7	3.4 ^{+3.1} _{-0.9}	32	28 (87.5)	9 (28.1)
33	11	UCL	μ Sco		9.9	17.2 ^{+0.9} _{-2.4}	54	52 (96.3)	14 (25.9)
34	32	Cham	Centaurus-Far		0.1	8.5 ^{+1.1} _{-1.3}	99	99 (100.0)	25 (25.3)
35	33	Cham	Chamaeleon-I		9.9	3.8 ^{+1.9} _{-0.9}	192	184 (95.8)	106 (55.2)
36	34	Cham	Chamaeleon-II		7.7	2.8 ^{+0.7} _{-1.1}	54	49 (90.7)	32 (59.3)

Notes. Col. 1: Running index for the listed clusters, ordered by decreasing age for the top 32 rows. The four clusters at the bottom are not included in our analysis but are listed here for completeness. Col. 2: SigMA label from [R23a](#). Col. 3: Position of clusters within traditional regions (TR), see Appendix A.1. Col. 4: Cluster names from [R23a](#) or [MR25](#). Col. 5: Stability threshold for each cluster used for quality criteria. Col. 6: Cluster ages and their uncertainties from [R23b](#) and [MR25](#) (PARSEC, BPRP). Cols. 7-10 list the number of sources for: all stellar members per cluster from the literature; used sources after applying stability cut for the position sample; all stellar members with available RV data; used sources after applying quality criteria for the velocity sample; the fraction of remaining sources relative to XYZ_{all} is given in brackets. The seven clusters marked with * are identified as “peculiar” concerning their relative motions within Sco-Cen (Sect. 5.2).

as given on the x-axis of Fig. 1, which results in the cumulative velocity dispersion over a time range of about 20 Myr.

To account for the different sample sizes of each cluster—several clusters contain only a handful of RVs (see Table A.2)—we use at each time-step a random subsample of 20 sources per cluster. This sub-sampling is done to avoid that the dispersion estimations are dominated by the sample size, which would naturally give more weight to the more massive clusters. The relatively low number of 20 is chosen to account for the fact that

several clusters have very low number statistics, especially when requiring good RV data quality. If a cluster has fewer than 20 members, then we randomly sample 20 data points with replacement. This up-sampling concerns nine out of the 32 clusters. We repeat this procedure 1000 times, and each time randomly draw another 20 stars from each cluster, which delivers a median and uncertainty for σ_{3D} at each time step, as plotted in Fig. 1. By iteratively adding random sub-samples of stellar members of each cluster one after another, we obtain an increase in velocity dis-

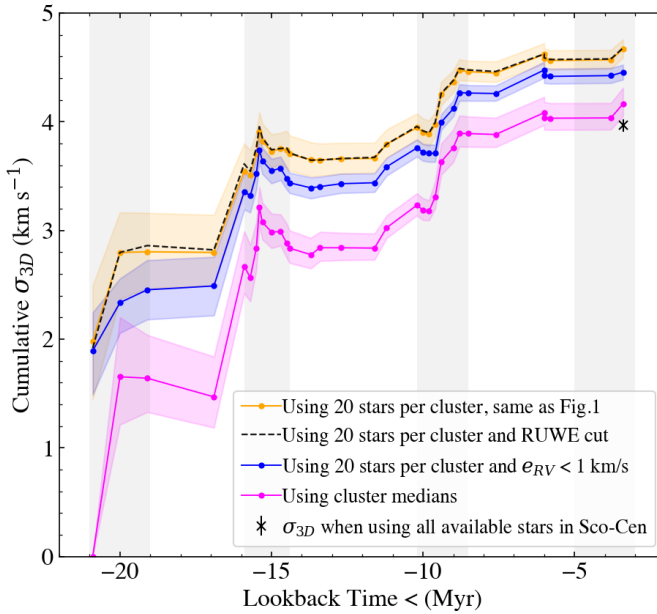


Fig. B.1. Temporal evolution of the cumulative 3D velocity dispersion. The upper orange curve is the same as in Fig. 1. The black, dashed curve shows the cumulative σ_{3D} when applying a cut on the *Gaia* RUWE parameter, to test the influence of binaries. The middle blue curve shows the cumulative σ_{3D} when applying an additional error cut at $e_{RV} \leq 1 \text{ km s}^{-1}$ on the stellar members of each cluster. The lower magenta curve shows the cumulative σ_{3D} when using the cluster medians. The black cross marks the total σ_{3D} as calculated from all stars in Sco-Cen with valid RV measurements. The error bars (shaded regions) show the 95% interquartile ranges (2σ).

dispersion, until the total velocity dispersion of the whole association is reached with $4.67 \pm 0.04 \text{ km s}^{-1}$.

As outlined in Sect. 4, we compare the total σ_{3D} from the sub-sampling approach to the total σ_{3D} when all available stellar members of the 32 clusters in Sco-Cen are used for its calculation. Hence, we use all stars in the 32 clusters that pass our quality criteria (i.e., 3128 out of 12,612), instead of 20 sub-samples from each cluster (the latter results in a sample of only 640 stars when the final time-step is reached). We bootstrap over the 3128 available sources with replacement 10,000 times. The mean of the bootstrap samples results in a 3D velocity dispersion of $3.96 \pm 0.03 \text{ km s}^{-1}$, which is about 0.7 km/s lower than the final value of the cumulative σ_{3D} . This difference might be caused by the undersampling of the velocity space when only using sub-samples. This might also increase the importance of individual measurement errors, which could inflate the final σ_{3D} . At the same time, the total velocity dispersion using all available stars might be dominated by the most massive clusters, which contain overall more stars with valid RV measurements.

To test the influence of RV measurement errors, we recalculate the cumulative σ_{3D} using two alternative data samples. First, we apply an additional RV error cut at $e_{RV} < 1 \text{ km s}^{-1}$ (and $e_{RV,w} < 1 \text{ km s}^{-1}$ if a source was observed by more than one survey). In some cases, this reduces the number of stellar members per cluster significantly; for 13 clusters, there are now fewer than 20 members available, and their numbers have to be up-sampled (for L134/L183, zero sources remain). Nevertheless, when comparing the resulting trend to the original one from Fig. 1, we find that the cumulative velocity dispersion increases similarly over time, while there is only a shift to overall lower values, on av-

erage about -0.2 km s^{-1} (see Fig. B.1, blue curve), and the total σ_{3D} results in $4.46 \pm 0.03 \text{ km s}^{-1}$.

Second, we calculate the cumulative velocity dispersion by using only the median *UVW* values of the clusters. With this approach, we remove any internal velocity scatter of each cluster, and we only focus on the more robust cluster velocities; so we get a measure of the lower limit of σ_{3D} . We randomly sample of the cluster medians and their uncertainties (assuming Gaussian errors) to get a measure of uncertainty for the clusters' cumulative σ_{3D} . Naturally, this approach results in low-number statistics, especially for the first few time-steps (at the start, only one velocity is used, from *e Lup*, hence, it is zero). Nevertheless, we find that the shape of the curve is similar, as highlighted in Fig. B.1 (magenta curve), with an average shift of about -0.5 to -0.6 km s^{-1} . The total 3D velocity dispersion of all 32 cluster medians results in $4.17 \pm 0.07 \text{ km s}^{-1}$.

Finally, we test the potential influence of unresolved binaries or multiples. We use *Gaia*'s Renormalised Unit Weight Error (RUWE), and a variable $\text{RUWE}_{\text{var-lim}}$ as given by Castro-Ginard et al. (2024, see their Appendix A). The suggested $\text{RUWE}_{\text{var-lim}}$ mainly depends on crowding at the location of a star in the field-of-view of *Gaia*. We repeat the calculation of the cumulative σ_{3D} by additionally requiring $\text{RUWE} < \text{RUWE}_{\text{var-lim}}$ and compare it to the cumulative σ_{3D} from Fig. 1. We find that the RUWE cut does not make a significant difference (Fig. B.1, black, dashed line). Overall, we only find small variations of about 0.03 km/s around the original trend. The total σ_{3D} when using the RUWE cut is then $4.68 \pm 0.05 \text{ km s}^{-1}$. We conclude that the influence of unresolved binaries is negligible concerning our selected *UVW* sample and that the influence of RV measurement errors is dominating any potential shifts of σ_{3D} .

Considering these different tests, we conclude that the present-day velocity dispersion of Sco-Cen is between 4.0 – 4.7 km s^{-1} . The measurement errors appear to influence the magnitude of the cumulative σ_{3D} , while the increasing trend, with the visible jumps and plateaus in between, appears to be unaffected and stays essentially the same.

B.2. Calculating the cumulative size of the region

To estimate the chronological build-up of Sco-Cen, we estimate the change in size (extent in pc) of the region, starting from the oldest to the youngest cluster (used Python packages: `sklearn.neighbors.kneighbors_graph`, `networkx`, `nx.single_source_dijkstra_path_length`), similar to the cumulative σ_{3D} . To estimate the size of a collection of subgroups at any age step, we determine the largest distance between any two sources at this step. Since Euclidean distances ignore the shape of Sco-Cen, we use a graph constructed from individual members (as nodes) to approximate the manifold of the association. We construct the graph via a k-neighbours graph in positional (*XYZ*) space and use Dijkstra's algorithm to compute shortest paths between any two sources in the graph (Dijkstra 1959). At each age step, we compute the maximum distance for all possible shortest paths between members of respective subgroups.

This is done again cumulatively, by starting with the stellar members from the oldest cluster, and adding at each age step stellar members of the next youngest cluster, while we use only stars that fulfil the stability criterion from Appendix A.4. We iterate over randomized subsamples per cluster of equal size to get an estimate of the uncertainty and to account for the different cluster sizes. We always add 30 randomly drawn stellar members of each cluster at each cumulative time step. For clusters

Table B.1. Central position and rest velocity of *SC15*.

Parameter	Median	Mean	STD
X (pc)	106.0 ± 0.6	105.0 ± 0.4	35.4
Y (pc)	-71.0 ± 0.6	-70.3 ± 0.3	25.1
Z (pc)	28.4 ± 0.3	28.6 ± 0.2	14.6
U (km/s)	-5.98 ± 0.11	-6.05 ± 0.07	2.38
V (km/s)	-19.99 ± 0.06	-20.04 ± 0.05	1.67
W (km/s)	-5.27 ± 0.04	-5.27 ± 0.03	1.15

Notes. The given Median and Mean are the averaged medians and means, which were calculated by bootstrapping 5000 times over the selected stellar members. The given errors are the standard deviations of the 5000 medians or means. The given STD is the average scatter of the XYZ or UVW distribution. The UVW_{LSR} values can be derived from UVW by adding the standard solar motion from Schönrich et al. (2010).

Table B.2. The difference in positions and motions when comparing the three reference points that are investigated in Figs. 3, 4, B.2, and B.3.

	<i>SC15</i> – <i>e Lup</i>	<i>SC15</i> – <i>ϕ Lup</i>	<i>e Lup</i> – <i>ϕ Lup</i>
ΔX (pc)	-13.4	-6.0	7.4
ΔY (pc)	4.9	-17.3	-22.2
ΔZ (pc)	-0.7	-11.7	-11.0
ΔCenter (pc)	14.3	21.7	25.9
ΔU (km/s)	-1.20	-1.26	-0.07
ΔV (km/s)	0.08	-0.22	-1.02
ΔW (km/s)	-1.19	-0.66	0.53
ΔSpeed (km/s)	1.87	1.44	1.15

with fewer members, we add the full set of cluster members of these sparse clusters (no up-sampling, no source appears more than once). Using at least 30 sources per cluster allows us to get a similar weight for sparser clusters compared to the richer clusters. Moreover, using fewer stars significantly reduces the computation time of Dijkstra. We iterate over this procedure 60 times, which delivers a median extent and its uncertainty per age step. With this method, the size of Sco-Cen at the present day cumulates in a value of 203^{+7}_{-12} pc.

B.3. Calculating cluster 3D bulk positions and motions

We use the Galactic Cartesian positions (XYZ) and motions (UVW or UVW_{LSR}) of the stellar members of each cluster to calculate the clusters' average properties in the 6D phase space. For XYZ , we only apply the stability cut as described above. For UVW , we use the stellar members that pass our additional quality criteria, with a particular focus on RVs (see Appendix A.4).

The Median and Mean of the clusters' 3D positions and motions are determined via bootstrapping with replacement (1000 times) by sampling from the stellar members of each cluster. The resulting averaged Median, Mean, and standard deviation (STD) from the bootstrapped distributions are used to determine the 6D properties of each cluster, reported in an online table (see Appendix C). The given uncertainties of Median, Mean, and STD are the standard deviation of the bootstrapped medians, means, and STDs. For our analysis, we use the medians and their uncertainties.

B.4. Testing different reference points

We investigate three points of reference in more detail, which are the two clusters *e Lup* and *ϕ Lup*, and *SC15*. The latter represents the bulk position and motion of older clusters with ages > 15 My. From these, we remove two sparse clusters, Pipe-North and *θ Oph*, since they show peculiar motions relative to the rest of the older clusters. Hence, we use eight clusters for the calculation of *SC15*, which are *e Lup*, Libra-South, US-foreground, *ϕ Lup*, *η Lup*, V1062-Sco, *ν Cen*, and *σ Cen*, containing a total of 7290 stellar members. To determine the centre and rest velocity, we use the Galactic Cartesian positions and motions of the stellar members of the eight clusters with applied quality criteria as outlined in Appendix A.4. This leaves 6659 stellar members in XYZ and 1288 in UVW space.

The median and mean position and velocity of *SC15* are obtained via bootstrapping (5000 times with replacement) over the selected stellar XYZ positions or UVW velocities. Table B.1 reports the averages of the bootstrapped medians, means, and standard deviations in XYZ and UVW . The given uncertainties are the standard deviations of the medians or means. For similar estimates, see P25 and MR25, while they used slightly different data, in particular concerning the selected RVs. The difference in position and motion between *e Lup*, *ϕ Lup*, and *SC15* are given in Table B.2.

Figures B.2 & B.3 show the resulting speed–time and radial-motion–distance relations, when using the two alternative reference points, *ϕ Lup* and *SC15*, compared to when using the oldest cluster, *e Lup*, as used in the main part of the paper (Figs. 3 & 4). We see similar, while slightly shallower, trends of speed with time and radial motion with distance.

B.5. Testing the robustness of the linear relations

In this section, we test the robustness of the speed–time and radial-motion–distance relations. In the main part of this paper, we use as a first choice the oldest cluster, *e Lup*, as a reference point. Alternatively, we also set *ϕ Lup* or the bulk motion of *SC15* as reference. We find similar correlations (see Figs. 3, 4, B.2, B.3 & Table 1), while these three reference points are generally at central locations with similar 3D space motions (see Table B.2).

We further test these relations by using each of the 32 clusters once as a reference point to calculate the relative speed or distance. In all cases, the reference cluster is excluded from the linear fit. We fit linear slopes to the resulting distributions in the speed–time and radial-motion–distance spaces, and we test the correlations with the coefficient of determination (r^2 -value), the Spearman rank correlation coefficient (SRCC; Spearman 1904; Daniel 1990), and the Pearson correlation coefficient (PCC; Pearson 1895). SRCC tests for monotonic relationships between two variables and ignores the scale, and PCC evaluates linear relationships using the physical scales.

For the speed–time relation, we find that the time-ordered case with *e Lup* as reference point delivers one of the cleanest linear trends, with the steepest slope and the highest r^2 , SRCC, and PCC values. We find that if using several of the older clusters as reference, we get similar linear trends compared to *e Lup*; these are *ϕ Lup*, *ν Cen*, *η Lup*, V1062-Sco, Sco-Sting, *ρ Lup*, *ρ Sco*, and UPK606 (all older than 13 Myr).

For the radial-motion–distance relation, we see a similar behaviour, while here *e Lup* stands out more clearly as the best fit with the steepest linear slope. Under ideal conditions, the best reference point (kinematic centre) does correspond to the steep-

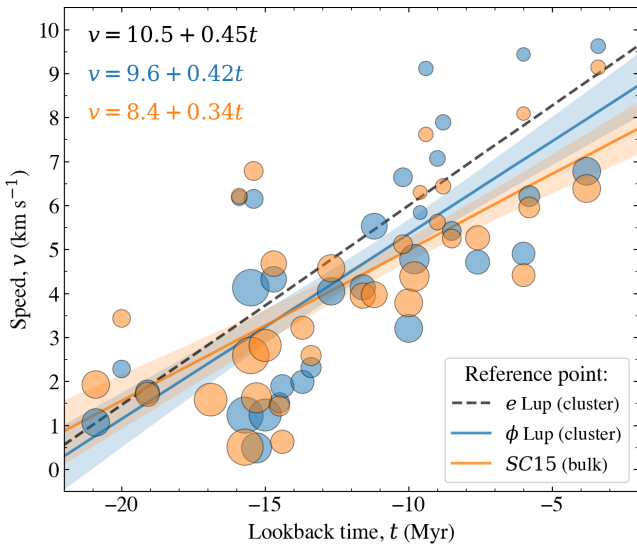


Fig. B.2. Speed–time relation, similar as Fig. 3, but with ϕ Lup (blue) or SC15 (orange) as reference points. For comparison, we also show the slope when e Lup is set as the reference point, from Fig. 3 (black, dashed line). The resulting median slopes are given in the upper left corner in the respective colours (see also Table 1). The shaded areas show the $1-\sigma$ uncertainties around the median slopes.

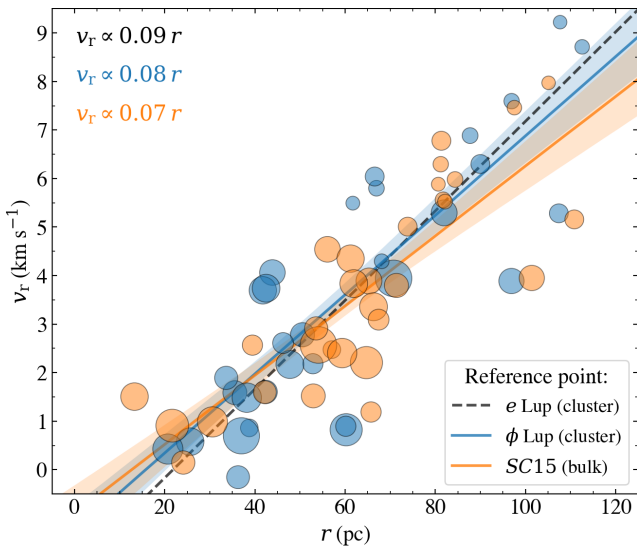


Fig. B.3. Radial-component–distance relation, similar as Fig. 4, but using ϕ Lup (blue) or SC15 (orange) as reference points. For comparison, we also show the slope when e Lup is set as the reference point, from Fig. 4 (black, dashed line). The resulting median slopes are given in the upper left corner in the respective colours (see also Table 1). The shaded areas show the $1-\sigma$ uncertainties around the median slopes.

est (and cleanest) positive slope for an approximately isotropic radial expansion pattern, because any offset from the true centre introduces non-radial components, which would flatten the correlation and increase the scatter.

That several of the older clusters appear to be also relatively good reference points, compared to e Lup, is consistent with the fact that the older clusters make up the bulk of Sco-Cen, they have generally similar space motions, and are located at central locations. The youngest of these older clusters is UPK606, with an age of about 13–14 Myr. This still fits a formation scenario, where feedback originating from the older clusters was mainly affecting younger clusters with ages younger than about 12 Myr,

which approximately marks the onset of the formation of cluster chains.

Finally, we test if the speed–time relation is indeed strongly linked to the formation time, since we find linear trends when using e Lup or several of the older clusters as reference points. To this end, we randomize the order of the time-axis, while we keep the speed-order as calculated for a given reference point. We set each of the 32 clusters once as a reference point, while the reference cluster is then removed from the correlation. We test if the time-ordered relations are significant by randomly shuffling the measured formation times (or cluster ages) on the x-axis. Additionally, we create a uniform distribution of times between the formation time limits of the Sco-Cen clusters, (-20.9, -3.4) Myr, to create cases that are within the physical boundaries of the observed case. This allows us to determine the linear regression statistics. For a more robust test, we determine the Spearman rank correlation coefficient (SRCC), which ranks the order of the values on the x and y-axis, and is now independent of the true physical scale.

We find that the results from the time-ordered cases—with e Lup, ϕ Lup, or SC15 as reference point—are only reproduced with a probability that is beyond 4σ . The positive linear correlation of time versus speed is not reproduced by the vast majority of the randomly ordered cases. About half of the random cases show negative trends (reversed slopes), which we also find when setting some of the mostly younger clusters as reference point (concerning Pipe-N, Musca-fg, η Cham, ϵ Cham, TWA-a,b, δ Sco, ν Sco, ρ Oph, B59). This test supports the hypothesis that the time-ordered behaviour of the motions in Sco-Cen, where younger clusters move faster compared to older ones, is unlikely created by a random process in which clusters would form independently from each other, but it lies at the bottom of the formation history of the region.

Appendix C: Online Material

We provide an online source catalogue (to be uploaded to Vizier), listing all stellar members of the investigated Sco-Cen clusters, including information on cluster labels and names, ages, derived parameters, and the used RV data. The final used RV value is either the measurement with the lowest RV uncertainty or the only available RV measurement. In column Ref, the respective RV References are listed, which indicate from which survey the measurement was taken. Additionally, we give the weighted mean and weighted standard deviation if a source has more than one RV measurement from different surveys. This gives information on possible multiples. We also list the VSCATTER parameter from APOGEE2 if available. Finally, the derived parameters, including XYZ and UVW , are listed as well (see also Sect. A.2). We flag the sources that pass our quality criteria in column used_stab and used_rv. The first is used for the 5D sample (used_stab = 1) and the second for the 6D sample (used_rv = 1).

The cluster properties are reported in a second online catalogue (to be uploaded to Vizier), containing median, mean, standard deviation, and their errors for the investigated parameters (as obtained via bootstrapping), which are the positions and motions (heliocentric and LSR corrected), including l , b , X , Y , Z , RV_{HEL} , RV_{LSR} , $v_{l,lsr}$, $v_{b,lsr}$, U , V , W , U_{LSR} , V_{LSR} , W_{LSR} . Moreover, we list the medians and uncertainties of the cumulative σ_{3D} and size for each time step, which were used to construct Figs. 1 and B.1.